





Functional dissection of neural circuitry using a genetic reporter for fMRI

Souparno Ghosh^{1,7}, Nan Li^{1,7}, Miriam Schwalm¹, Benjamin B. Bartelle¹, Tianshu Xie¹, Jade I. Daher^{1,2}, Urvashi D. Singh¹, Katherine Xie³, Nicholas DiNapoli³, Nicholas B. Evans³, Kwanghun Chung^{1,2,3,4,5} and Alan Jasanoff^{1,2,6}  

The complex connectivity of the mammalian brain underlies its function, but understanding how interconnected brain regions interact in neural processing remains a formidable challenge. Here we address this problem by introducing a genetic probe that permits selective functional imaging of distributed neural populations defined by viral labeling techniques. The probe is an engineered enzyme that transduces cytosolic calcium dynamics of probe-expressing cells into localized hemodynamic responses that can be specifically visualized by functional magnetic resonance imaging. Using a viral vector that undergoes retrograde transport, we apply the probe to characterize a brain-wide network of presynaptic inputs to the striatum activated in a deep brain stimulation paradigm in rats. The results reveal engagement of surprisingly diverse projection sources and inform an integrated model of striatal function relevant to reward behavior and therapeutic neurostimulation approaches. Our work thus establishes a strategy for mechanistic analysis of multiregional neural systems in the mammalian brain.

Optical measurements of signaling dynamics in well-defined neural circuit components are possible by combining invasive optical imaging methods with fluorescent probes such as the genetically encoded calcium sensor GCaMP¹, but these approaches only operate over limited volumes. To permit measurements of circuit-level processing on a brain-wide scale, we sought to construct an analog of GCaMP that could be detected by noninvasive imaging methods such as functional magnetic resonance imaging (fMRI)^{2,3}, functional photoacoustic tomography⁴ or functional ultrasound⁵. These methods usually operate by monitoring blood flow changes evoked nonspecifically by neural population activity⁶. We reasoned that a molecular probe designed to couple the intracellular signaling activity of genetically targeted cells to hemodynamic changes could form the basis of cell-specific functional neuroimaging, provided that output from the probe could be adequately distinguished from endogenous hemodynamic signatures (Fig. 1a). We refer to this concept as hemogenetic imaging, because it employs a genetic probe to produce a hemodynamic readout.

We chose a molecular basis for hemogenetic reporters by considering contributions to normal neurovascular coupling in mammalian brains. Although many signaling pathways have been implicated⁷, a particularly strong effect is mediated by neuronal nitric oxide synthase (nNOS). This enzyme catalyzes local formation of the cell-permeable gaseous vasodilator nitric oxide (NO) during neural signaling. Optogenetic stimulation of nNOS-positive neurons in the brain produces robust hemodynamic responses that scale with stimulus strength⁸, and pharmacological nNOS inhibition substantially reduces fMRI responses to sensory stimuli^{9,10}. Neuronal signaling activates nNOS via its association with calcium-bound calmodulin, the same protein domain that actuates fluorescent protein-based calcium sensors¹¹. These considerations led us to design hemogenetic probes termed ‘nitric oxide synthases

for targeting image contrast’ (NOSTICs) by engineering an nNOS isoform that retains calcium sensitivity but that can be selectively manipulated by drugs that do not perturb intrinsic hemodynamic responses.

In this work, we sought to establish the principle of hemogenetic imaging with NOSTIC probes and begin to explore applications in neurobiology. Our results comprise protein engineering of the NOSTIC reporters, *in vitro* and *in vivo* validation studies and functional analysis of neural circuitry in rodent brains using the approach. We demonstrate that hemogenetic fMRI provides brain-wide information about neural information flow that can be combined with complementary data to yield insights into brain mechanisms.

Results

Construction and validation of hemogenetic reporters. First-generation NOSTICs, called NOSTIC-1 and NOSTIC-1P, were created by replacing the catalytic domain of nNOS with corresponding residues from inducible nitric oxide synthase (iNOS), an immune-associated nitric oxide synthase (NOS) variant that displays distinctive sensitivity to inhibitors (Fig. 1b and Supplementary Table 1)¹². NOSTIC-1P further contains the PDZ domain of nNOS, which directs association with synaptic proteins¹³, and which NOSTIC-1 lacks. These probes therefore combine NOS activity with the possibility of cellular or subcellular targeting.

Calcium dependence and pharmacological sensitivity of the NOSTIC probes were examined in cell culture. Both NOSTIC-1 and NOSTIC-1P express robustly in HEK293 cells, with primarily cytosolic expression consistent with previous reports¹⁴ (Supplementary Fig. 1). To evoke cytosolic calcium elevations similar to those observed in a variety of signal transduction mechanisms, we applied the widely used calcium ionophore A23187. Stimulation with this

¹Department of Biological Engineering, Massachusetts Institute of Technology, Cambridge, MA, USA. ²Department of Brain & Cognitive Sciences, Massachusetts Institute of Technology, Cambridge, MA, USA. ³Institute for Medical Engineering & Science, Massachusetts Institute of Technology, Cambridge, MA, USA. ⁴Department of Chemical Engineering, Massachusetts Institute of Technology, Cambridge, MA, USA. ⁵Broad Institute of MIT and Harvard, Massachusetts Institute of Technology, Cambridge, MA, USA. ⁶Department of Nuclear Science & Engineering, Massachusetts Institute of Technology, Cambridge, MA, USA. ⁷These authors contributed equally: Souparno Ghosh, Nan Li. ✉e-mail: jasanoff@mit.edu

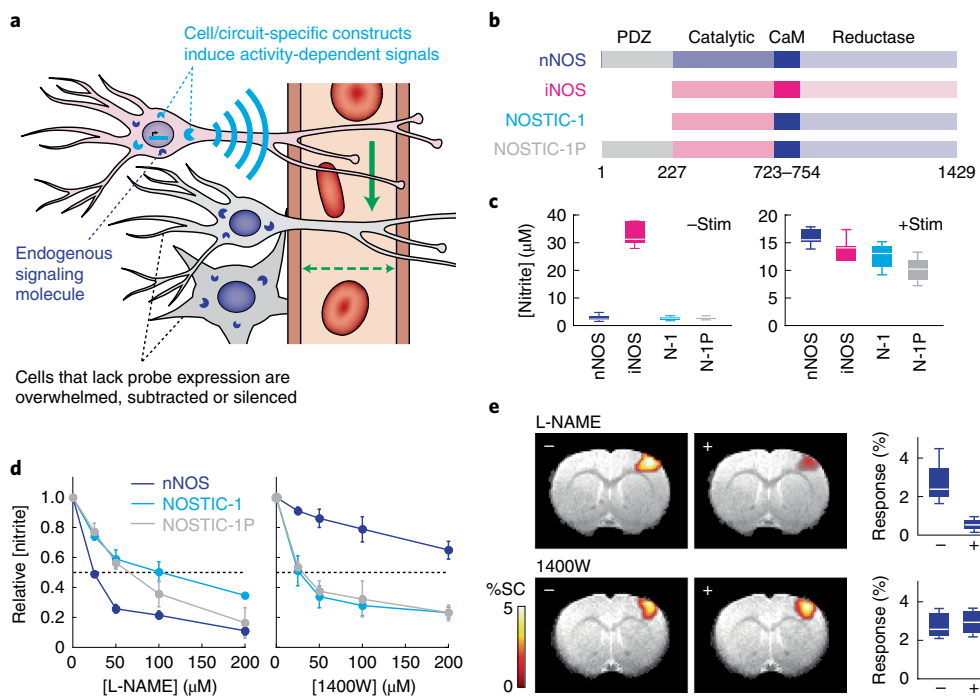


Fig. 1 | Principle of hemogenetic imaging with NOSTICs. **a**, Hemogenetic imaging involves detection of localized changes in blood flow or volume (green arrows) induced by genetically encoded activity reporters (cyan) analogous to fluorescent probes such as GCaMP. Hemogenetic reporters signal to nearby blood vessels (cyan wireless symbol), inducing hemodynamic image contrast that can be detected by fMRI and related methods. Endogenous drivers of activity-dependent signals (dark blue) are suppressed, silenced or subtracted. **b**, NOSTIC-1 and NOSTIC-1P reporters are calcium-dependent chimeric enzymes that combine the catalytic domain of iNOS with calmodulin-binding (CaM) and reductase domains of nNOS; NOSTIC-1P also contains the synapse-targeting nNOS PDZ domain. **c**, Measurement of nitrite formation following NO release from cells expressing nNOS, iNOS, NOSTIC-1 (N-1) and NOSTIC-1P (N-1P) in absence (left) or presence (right) of stimulation using the Ca^{2+} ionophore A23187. Calcium-dependent induction of nNOS, N-1 and N-1P is significant with two-sided t -test $P \leq 0.0018$ ($n = 3$). Error bars denote s.e.m. of three measurements. **d**, Activity measurements titrated with the nNOS-selective inhibitor L-NAME (left) or iNOS-selective inhibitor 1400W (right). Horizontal dashed lines denote half-maximal activity levels, at which IC_{50} values of the inhibitors apply. Error bars denote s.e.m. of three measurements each. **e**, Sensory-driven fMRI signals in rat cortex visualized with or without NOS inhibition using 50 mg kg^{-1} L-NAME (top, $n = 4$) or 25 mg kg^{-1} 1400W (bottom, $n = 3$). Images display percent signal change (%SC, color bar) superimposed on an anatomical scan. Box plots denote median (center line), first quartiles (boxes) and full range (whiskers) of fMRI responses observed in S1 forelimb region, over animals. The L-NAME effect is significant with two-sided t -test $P = 0.04$.

drug evokes comparable levels of NO production by both NOSTICs and nNOS (Fig. 1c). Calcium-dependent NO increases for nNOS, NOSTIC-1 and NOSTIC-1P are all significant with t -test $P \leq 0.0018$ ($n = 3$). The nNOS-selective inhibitor L-nitroarginine methyl ester (L-NAME) blocks this effect with a concentration producing 50% inhibition (IC_{50}) of $20 \mu\text{M}$ for nNOS, but more than $50 \mu\text{M}$ for the NOSTICs (Fig. 1d). In contrast, the iNOS-specific blocker 1400W inhibits NOSTICs with IC_{50} values of about $25 \mu\text{M}$, with over tenfold lesser effect on nNOS. Stimulation and pharmacological blockade of NOSTIC-dependent NO production could also be observed in a neuronal cell line (Extended Data Fig. 1), indicating that NOSTICs are suitable for brain applications and functional in multiple cell types. Importantly, drugs that respectively inhibit nNOS and NOSTICs produce sharply different effects on endogenous fMRI responses, as tested using a sensory stimulation paradigm in rats (Fig. 1e, Extended Data Fig. 2 and Supplementary Fig. 2). L-NAME injection reduces the primary somatosensory cortex (S1) response to electrical forepaw stimulation by $2.42 \pm 0.53\%$ (significant with paired t -test $P = 0.04$, $n = 4$), but 1400W produces virtually no change ($0.15 \pm 0.07\%$ increase, paired t -test $P = 0.29$, $n = 3$). These results thus demonstrate a basis for drug-dependent selective imaging of NOSTIC reporters by hemodynamic neuroimaging.

To validate the probes in vivo, we examined the ability of NOSTIC-expressing cells to induce activity-dependent hemodynamic imaging signals following xenotransplantation into rat

brains. Only NOSTIC-1 was used for these studies, because of its greater calcium-dependent NO production compared with NOSTIC-1P in vitro. HEK293 cells stably expressing NOSTIC-1 were implanted into the striatum and imaged using a 9.4T magnetic resonance imaging (MRI) scanner during stimulation with $10 \mu\text{M}$ A23187 (Fig. 2a and Supplementary Fig. 3). Calcium ionophore treatment induces robust blood oxygen level-dependent (BOLD) fMRI responses in the neighborhood of the cells (Fig. 2b). In contrast, control experiments performed in the presence of the NOSTIC inhibitor 1400W or using cells that express green fluorescent protein (GFP) in place of NOSTIC-1 result in negligible fMRI responses. The A23187-induced NOSTIC signal persists for ~ 10 min, likely reflecting slow washout of the ionophore (Fig. 2c), and results in a mean signal increase of $6.2 \pm 1.4\%$ (Fig. 2d) that is significantly greater than both controls (t -test $P \leq 0.001$, $n = 5$). The full-width at half-height of the NOSTIC response averages $1.4 \pm 0.1 \text{ mm}$, similar to the mean xenograft diameter of $1.8 \pm 0.5 \text{ mm}$ (Extended Data Fig. 3). This implies that the point-spread function width of NOSTIC-dependent fMRI signals is comparable to or less than the value of $\sim 1 \text{ mm}$ reported for intrinsic BOLD fMRI responses at 9.4T (ref. 15). These experiments show that stimulus-induced NO production by implanted cells is sufficient for induction of local BOLD responses and demonstrate that NOSTIC-1 can selectively report the activation of probe-expressing cells in fMRI.

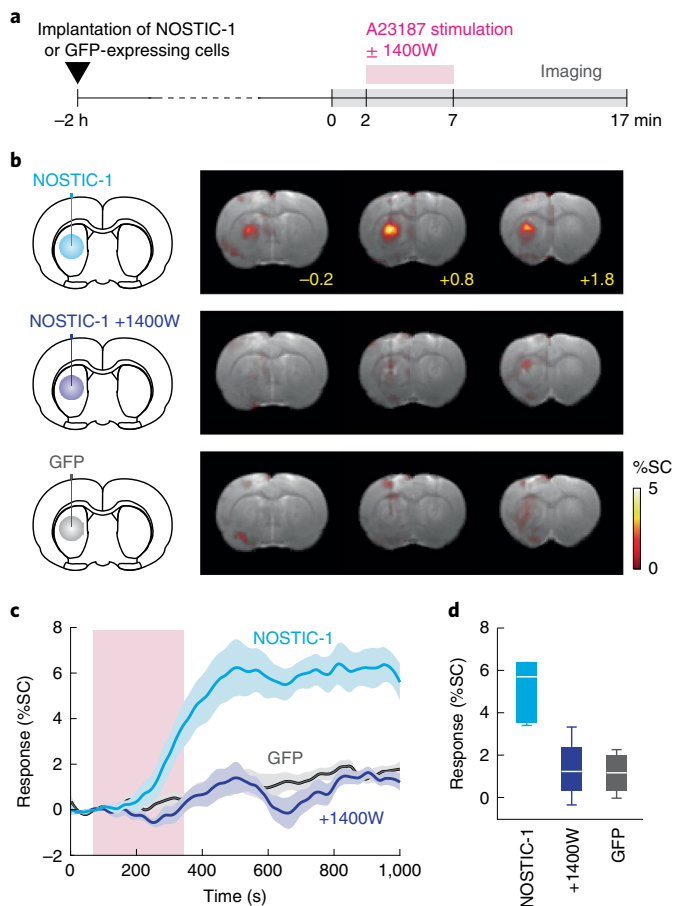


Fig. 2 | NOSTIC-1 reports activation of genetically modified cells in vivo.

a, Timeline of intracranial implantation and imaging of NOSTIC-expressing or control cells stimulated by infusion of A23187 in the absence or presence of the NOSTIC-1 inhibitor 1400W. **b**, BOLD MRI contrast changes induced by A23187-mediated stimulation: (top) NOSTIC-1-expressing cells without 1400W, (middle) NOSTIC-1 cells with 1400W, (bottom) GFP-expressing cells without 1400W. Each panel shows three coronal slices within 1 mm of the cell implantation site with a percent signal change (%SC) map overlaid on a representative anatomical scan. **c**, Mean time courses of MRI signals in ROIs centered around the cell implantation sites in **b** for animals implanted with NOSTIC-1-expressing cells in the absence (cyan) and presence (dark blue) of 1400W, and control GFP cells without 1400W (dark gray). Stimulation period is denoted by light magenta box; shading denotes s.e.m. of $n = 6$ (NOSTIC-1), $n = 4$ (+1400W) or $n = 4$ (GFP). **d**, Average signal change amplitudes corresponding to the data in **c**. Box plots denote median (center line), first quartiles (boxes) and full range (whiskers) of response amplitudes across animals. The NOSTIC-1 response without 1400W is statistically significant with two-sided t -test $P = 0.006$ ($n = 6$), while the control responses are not significant with two-sided t -test $P \geq 0.11$ ($n = 4$).

Functional imaging of targeted neural circuitry with NOSTIC.

We next applied NOSTIC-1 to analyze neural circuit function in the striatum, a major hub for integration of sensory, motor and affective input from remote brain areas, and a target of deep brain stimulation (DBS) therapies in the clinic. Understanding which connections provide active inputs during behaviorally relevant tasks or stimuli is essential to formulating circuit-level models of striatal function. Anatomical connections of the striatum have been studied by applying viral vectors that undergo axonal transport and express fluorescent proteins detectable in postmortem microscopy^{16–19}; functional

assessment of the projections should therefore become possible by using similar vectors to drive expression of NOSTIC-1, followed by functional imaging. We used this approach to measure striatal input during electrical stimulation of the lateral hypothalamus (LH)²⁰, a widely used addiction model in rodents and an exploratory DBS treatment for refractory obesity and depression in patients^{21,22}. A specific unanswered question in this context is whether striatal activation due to LH stimulation arises primarily from excitation of striatal afferents passing through this region²³, or whether alternative circuit-level mechanisms might help explain striatal responses and associated behavioral effects.

To label direct striatal afferents with NOSTIC-1, we constructed a herpes simplex virus (HSV) vector encoding NOSTIC-1 and mCherry (HSV-hEF1 α -NOSTIC-IRES-mCherry). Similar vectors have been shown to produce persistent expression following retrograde transport from sites of injection in the rodent brain²⁴, implying that NOSTICs delivered this way should report the activity of neural populations that provide direct presynaptic input to striatal cells from throughout the brain. After confirming the ability of HSV-hEF1 α -NOSTIC-1-IRES-mCherry to induce intracellular calcium-dependent NO production in cultured cells (Extended Data Fig. 4), we injected the virus into the anterior central caudate putamen (CPU) of six rats implanted with electrodes targeted to the medial forebrain bundle region of LH (Fig. 3a). Histological results confirmed that virally driven probe expression does not strongly correlate with inflammatory markers (Supplementary Fig. 4). Three weeks after viral transduction, animals were sedated with medetomidine and imaged by BOLD fMRI during alternating blocks of LH stimulation and rest, first before and then after systemic treatment with the NOSTIC-1 inhibitor 1400W. These data permit identification of NOSTIC-specific signals based on the difference between fMRI responses observed in the absence versus presence of the drug (Fig. 3a), reflecting presynaptic functional input to CPU during LH stimulation.

A broad distribution of brain areas is activated both before and after 1400W treatment (Fig. 3b, Extended Data Fig. 5 and Supplementary Fig. 2), but difference maps denoting fMRI amplitudes specifically attributable to NOSTIC-expressing cells reveal a limited set of peaks (Fig. 3c). These maps are calculated by subtracting response time courses computed in unbiased fashion for each voxel before versus after 1400W treatment, but a more rigid fMRI analysis that assumes a fixed hemodynamic response for all voxels also produces similar results (Supplementary Fig. 5). In both analyses, 1400W-dependent difference peaks are largely absent in data from rats transduced with the control vector HSV-hEF1 α -mCherry in place of the NOSTIC-1 vector (Fig. 3c, Extended Data Fig. 6 and Supplementary Fig. 5). Difference signals observed in the maps of Fig. 3c reflect 1400W-dependent scaling of the time courses of underlying fMRI signals (Fig. 3d and Extended Data Fig. 7), which in some brain regions display a characteristic extended profile²⁵ shown previously to parallel striatal electrophysiological recordings²⁶. Similarity of time courses observed in the absence versus presence of 1400W indicates that NOSTIC-dependent hemogenetic signals are temporally similar to endogenous BOLD responses, suggesting a shared mechanistic basis for intrinsic and NOSTIC-mediated fMRI signals.

Difference signals from each animal were further analyzed over eight anatomically defined regions of interest (ROIs) ipsilateral to the LH stimulation site, focusing on areas in which peak effects of Fig. 3c are observed. Average fMRI difference amplitudes in several of these ROIs are substantially higher in NOSTIC animals than in rats transduced with the control mCherry-expressing HSV (Fig. 3e), providing a basis for statistically robust analysis of differences between the two conditions. No significant ROI-level difference signals are observed in the controls (paired t -test $P \geq 0.08$, $n = 5$), but 1400W-dependent fMRI signal differences from the NOSTIC

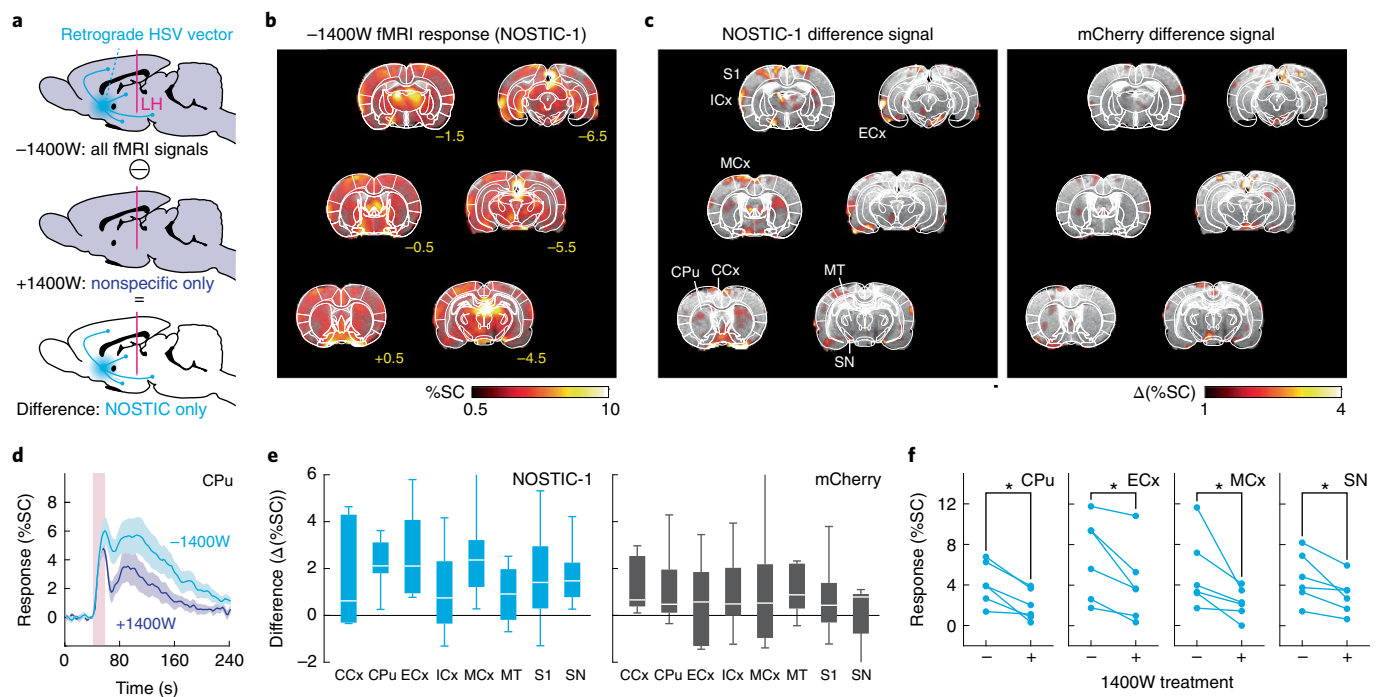


Fig. 3 | Hemogenetic functional imaging of striatal circuitry. **a**, Approach for hemogenetic analysis of striatal circuit function: An HSV vector delivers NOSTIC-1 to neurons presynaptic to a striatal injection site (cyan). Functional imaging during stimulation via an LH-targeted electrode (magenta) performed in absence (top) and presence (middle) of inhibition with 1400W, which suppresses NOSTIC-mediated fMRI signals but not endogenous nonspecific fMRI responses (purple). NOSTIC-specific responses to DBS are obtained by subtraction (bottom). **b**, Average fMRI responses to LH stimulation in the -1400W condition, among six animals infected with NOSTIC-encoding HSV. Significant responses with F -test $P \leq 0.01$ are shown. **c**, Mean of fMRI response amplitude differences between -1400W and +1400W conditions observed for animals infected with NOSTIC-1 ($n = 6$) or mCherry-only ($n = 5$) viruses; select ROIs are labeled. **d**, Average time courses of fMRI signals observed in CPU under each condition. Pink box denotes the stimulation period. Shading denotes s.e.m. over six animals. **e**, Difference signal amplitudes for NOSTIC-1 (left, $n = 6$) or mCherry control animals (right, $n = 5$) in eight ROIs labeled in **c** (also see Supplementary Fig. 1). Box plots denote median (center line), first quartiles (boxes) and full range (whiskers) over multiple animals. **f**, Absolute fMRI response amplitudes illustrating consistent 1400W-dependent responses in CPU, ECx, MCx and SN, all significant with two-sided paired t -test $*P \leq 0.05$ ($n = 6$).

animals are statistically significant with paired t -test $P \leq 0.05$ ($n = 6$) in CPU ($2.2 \pm 0.5\%$ signal difference), entorhinal cortex (ECx, $2.6 \pm 0.8\%$), motor cortex (MCx, $2.9 \pm 1.1\%$) and substantia nigra (SN, $1.7 \pm 0.6\%$) (Fig. 3f and Extended Data Fig. 8). When fMRI response amplitude differences are expressed as percent change in pre-1400W signal (Extended Data Fig. 9), NOSTIC results in CPU, ECx, MCx and SN are also especially pronounced, with 1400W-induced reductions of 38–51% and paired t -test $P \leq 0.008$ ($n = 6$) in each case. Group-averaged 1400W-dependent fMRI amplitude differences are significantly greater in NOSTIC animals than in controls when compared across all ROIs examined (paired t -test $P = 0.046$, $n = 8$ ROIs) or over CPU, ECx, MCx and SN in particular (paired t -test $P = 0.0065$, $n = 4$ ROIs), providing further evidence for specificity of the results. NOSTIC-based hemogenetic imaging results thus identify multiple brain regions that provide consistent presynaptic contributions to the striatum during LH stimulation, including cortical sources with striatal afferents that do not traverse the DBS target site¹⁶.

Confirmation of hemogenetic results using other techniques. To assess alignment of the hemogenetic fMRI data with established anatomical and functional measurement techniques, we began by comparing NOSTIC imaging results with structural connectivity patterns revealed by retrograde viral tracing. Unbiased brain-wide histological analysis following tissue clearing²⁷ in animals infected by CPU injections of an mCherry-encoding HSV shows prominent fluorescence corresponding to cells in CPU, ECx, MCx, medial

thalamus (MT) and SN (Fig. 4a); additional features are observable in individual tissue slices (Fig. 4b). As expected, the brain regions most heavily labeled by striatal injection of the HSV vector thus include the sources of striatal input most reliably identified by NOSTIC-based fMRI studies.

To complement this purely anatomical validation with a functional readout, we combined HSV-mCherry retrograde tracing from CPU with measurements of activity-dependent *c-Fos* protein expression induced by the same stimulus protocol used in the fMRI experiments. We predicted that striatal input regions identified in the NOSTIC experiments of Fig. 3 would show the greatest density of *c-Fos*-positive cells also labeled by HSV-mCherry. Microscopy images confirm that doubly stained cells are indeed much more readily observed in CPU, ECx, MCx and SN (Fig. 4c) than in two brain areas, cingulate cortex (CCx) and MT, where NOSTIC signals are not statistically significant (Fig. 4d). Results of this analysis are quantified in Fig. 4e and indicate densities of *c-Fos*-positive HSV-labeled cells from 5.3 to 25 cells per mm^2 in CPU, ECx, MCx and SN, but only 0.066 and 1.2 cells per mm^2 in CCx and MT, respectively. Across animals, *c-Fos*/mCherry-labeled cell densities in CPU and SN in particular are significantly higher than values in CCx and MT (t -test $P \leq 0.016$, $n = 4$). Comparison of double-labeled cell densities with NOSTIC signals in the six regions analyzed (Fig. 4f) reveals positive, though not statistically significant, correlations of $R = 0.3$ when all six brain areas are included or 0.8 when SN is omitted; treatment of SN as an outlier may be justified by the fact that this small structure is more susceptible to partial volume effects

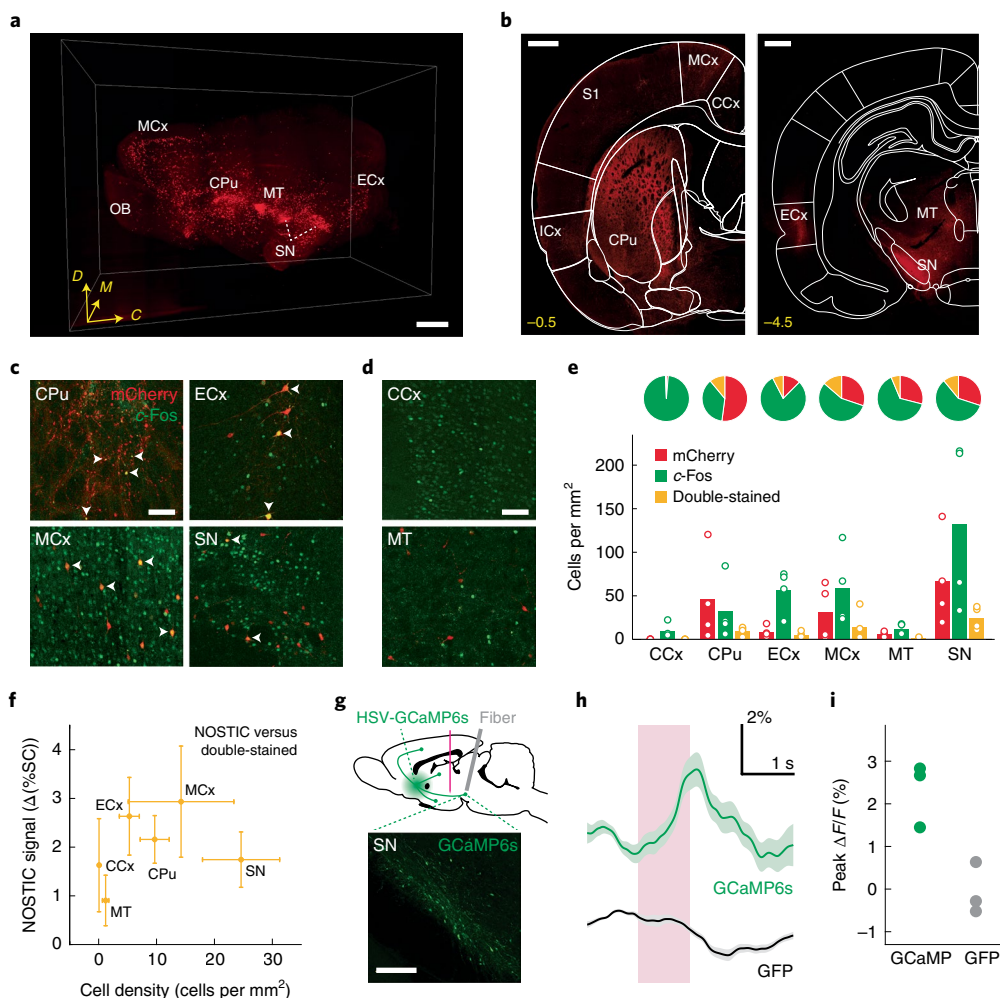


Fig. 4 | Alternative measures of striatal input. **a**, Unbiased fluorescence mapping in a cleared brain hemisphere imaged after HSV-mCherry delivery to rat CPu. Areas with substantial mCherry expression are labeled, along with the olfactory bulb (OB), for reference. Dorsal (D), medial (M) and caudal (C) directions denoted. Scale bar, 2 mm. **b**, HSV-driven mCherry expression in specific slices, with anatomical ROIs labeled on the atlas overlay (white) and bregma coordinates in yellow. Scale bars, 1 mm. **c**, Visualization of *c-Fos* protein expression (green) and HSV-directed mCherry expression (red) in animals infected with NOSTIC-encoding HSV and stimulated as in the fMRI experiments. Arrowheads indicate costained cells. Scale bar, 100 μ m. **d**, Data from two regions without significant NOSTIC responses, showing *c-Fos* staining only in CCx (top) and nonoverlapping *c-Fos* and mCherry staining in MT (bottom). Scale bar, 100 μ m. **e**, Quantification of mCherry (red), *c-Fos* (green) and overlapping (yellow) staining densities in six ROIs (bar graphs), also showing relative frequencies at top (pie charts); $n = 4$ animals in each case. **f**, Comparison of mCherry and *c-Fos* double-stained cell densities versus NOSTIC amplitudes in six ROIs. Error bars denote s.e.m. of $n = 4$ (horizontal) or $n = 6$ (vertical). **g**, Schematic of photometry experiments, showing striatal HSV-GCaMP6s injection site (green), LH electrode (magenta) and fiber placement (gray) in a sagittal section at top, with histological visualization of GCaMP6s-expressing SN neurons at bottom. Scale bar, 200 μ m. **h**, Representative photometry traces indicating relative change in fluorescence ($\Delta F/F$) from striatally projecting SN cells in a GCaMP6s-expressing animal (top) and a GFP-expressing control (bottom). Pink box denotes LH stimulation period. Shading, s.e.m. over 40 stimulus presentations. **i**, Photometry response amplitudes recorded from three test and control animals, as in panel **h** (difference significant with *t*-test $P = 0.028$).

in the fMRI analysis. In any case, the broad agreement between *c-Fos* histochemistry and NOSTIC results we observed provides further experimental support for the hemogenetic results of Fig. 3 and suggests that larger NOSTIC-mediated fMRI amplitudes on average reflect greater densities of stimulus-activated neurons in each brain region.

To support the NOSTIC-based fMRI results using a more dynamic activity measure, we used a retrogradely transported HSV vector to express the genetically encoded fluorescent calcium sensor GCaMP6s in place of the NOSTIC-1 probe; the virus was again introduced into CPu and fiber photometry was applied to measure from striatally projecting SN neurons during LH-targeted DBS (Fig. 4g). Photometry recordings reveal stimulus-evoked calcium

transients that are absent when a GFP-encoding virus is used in place of HSV-GCaMP6s (Fig. 4h and Supplementary Fig. 6). Mean fluorescence change amplitudes of 2.2% and 0.1% are observed in GCaMP6s and GFP conditions, respectively (Fig. 4i). This difference is significant with *t*-test $P = 0.028$ ($n = 3$), and confirms the presence of an LH stimulus-activated neural population that projects from SN to CPu. Although we did not perform photometry on further striatal input regions identified by the hemogenetic imaging approach, the SN-to-CPu result is particularly important because of longstanding uncertainty about whether striatal input evoked by LH stimulation travels directly from the DBS site or indirectly, via the midbrain²³. NOSTIC, photometry and *c-Fos* results all indicate that the indirect route is at least partially involved.

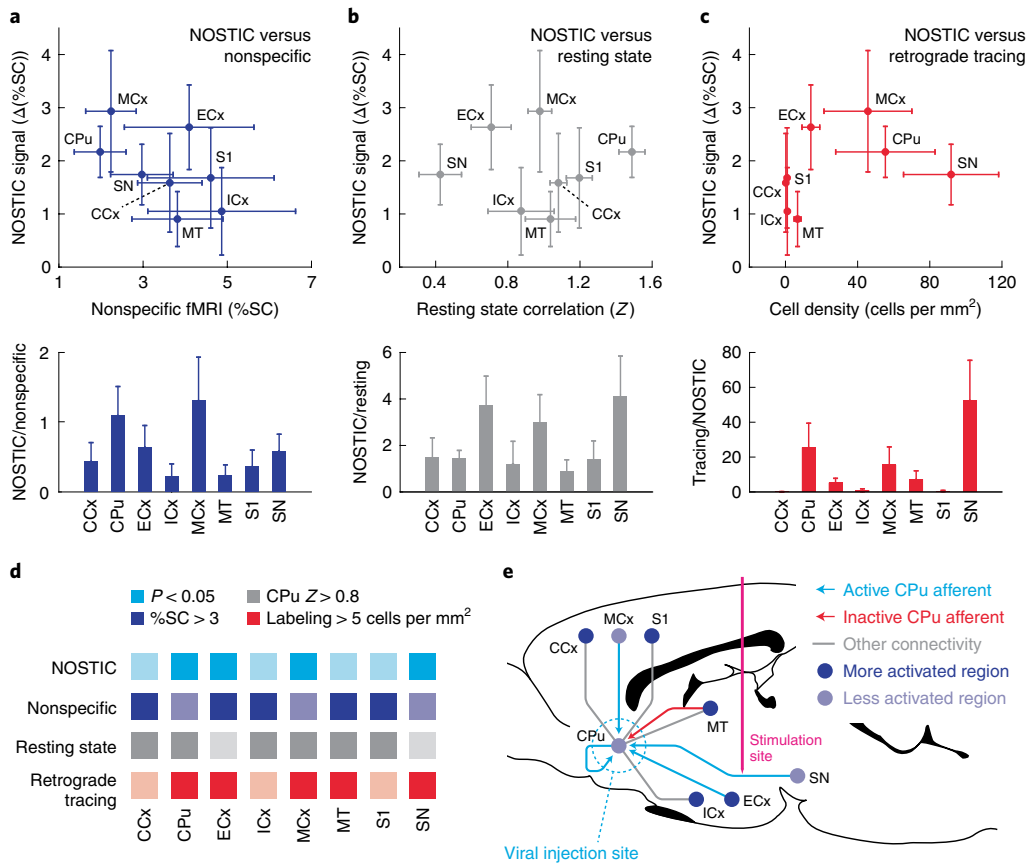


Fig. 5 | Multimodal analysis of striatal input/output relationships. **a**, Comparison of NOSTIC signal amplitudes versus nonspecific fMRI responses to LH stimulation (both $n = 6$) recorded in the presence of 1400W (top). Ratios of NOSTIC to nonspecific signals shown at bottom. **b**, Comparison of NOSTIC signals ($n = 6$) versus Z-transformed resting state correlation coefficients ($n = 4$) at top, with ratios shown at bottom. **c**, Comparison of NOSTIC signals ($n = 6$) versus retrogradely traced mCherry-labeled cell densities ($n = 4$) at top, with ratios shown at bottom. Error bars in panels **a–c**, s.e.m., computed by propagation of error from group data (bottom only); see text for additional statistics. **d**, Summary of hemogenetic imaging, nonspecific fMRI, resting state connectivity and anatomical connectivity amplitudes across eight ROIs (left); more saturated colors denote statistically significant NOSTIC responses (cyan), mean nonspecific fMRI responses $>3\%$ (indigo), resting state correlations to CPU with mean Z values >0.8 (gray) and retrograde labeling of CPU-projecting regions containing >5 cells per mm^2 (red). **e**, Sagittal brain diagram schematizing striatal circuitry consistent with the combined results. Circles denote DBS-evoked activation levels; lines denote functional connectivity defined by hemogenetic imaging (cyan), resting state analysis (gray, nondirectional) or histology (red).

Comparing hemogenetic imaging with complementary measures. Although NOSTIC-based hemogenetic imaging in its current form requires two measurements, the resulting two datasets provide information not only about probe-expressing neural populations, but also about intrinsic population activity. By comparing NOSTIC-mediated responses with intrinsic nonspecific fMRI signals recorded from the same animals in the presence of 1400W, the response profiles of neural populations with differing synaptic relationships to the striatum can be distinguished (Fig. 5a). NOSTIC and nonspecific fMRI signals are weakly negatively correlated, with $R = -0.56$ ($P = 0.15$, $n = 8$ ROIs). Several regions—CCx, insular cortex (ICx), MT and S1—show statistically significant nonspecific fMRI responses to LH stimulation (t -test $P \leq 0.045$, $n = 6$) but not significant NOSTIC responses. Although NOSTIC signals in ECx and MT are significantly different from each other ($P = 0.022$), the nonspecific imaging signals in these regions do not differ; conversely, although intrinsic fMRI signals differ significantly between CCx versus SN, CPU versus MT and MCx versus MT ($P \leq 0.044$), NOSTIC signals among these regions could not be statistically discriminated. Ratios of mean NOSTIC signals to intrinsic fMRI signals are highest in CPU (1.1 ± 0.4 , significant with t -test $P = 0.047$) and MCx (1.3 ± 0.6), suggesting that a particularly high proportion

of stimulus-responsive cells in these two areas provide direct input to striatal HSV infection sites. The lowest relative NOSTIC signals are observed in ICx (0.22 ± 0.19) and MT (0.24 ± 0.15), suggesting that stimulus responses in these regions are elicited by striatal output or by pathways that are not directly related to striatal activity. These results collectively show that intrinsic and NOSTIC-mediated fMRI measures convey distinct information about brain responses to LH stimulation.

We next considered whether hemogenetic measurements of circuit-level functional connectivity are similar to traditional ‘resting state’ functional connectivity assessments derived from cross-correlation of regional fMRI time courses in the absence of tasks or stimuli²⁸. To explore this question, we acquired resting state fMRI data from four additional animals and computed Z-transformed correlation coefficients relating CPU time courses to each ROI (Fig. 5b and Extended Data Fig. 10). All eight ROIs display statistically significant nonzero Z-scores (t -test $P \leq 0.001$, $n = 4$), but the relative strengths of each connection differ from those observed using the hemogenetic technique ($R = -0.017$, $P = 0.97$, $n = 8$ ROIs). While ECx and SN both exhibit significant NOSTIC signals (t -test $P \leq 0.028$, $n = 6$), these two regions also display the lowest resting state functional connectivity to CPU of the eight regions examined,

with the SN Z-score significantly below those from all other regions except ECx (t -test $P \leq 0.018$, $n = 4$). ECx and SN display the highest ratios of average NOSTIC signal to resting state Z, with values significantly nonzero in ECx in particular (t -test $P = 0.032$, $n = 6$). The results therefore dissociate NOSTIC-based measurements from conventional resting state connectivity and show that resting state analysis does not emphasize monosynaptic relationships engaged during LH-targeted stimulation.

The HSV-mCherry labeling data of Fig. 4, which indicate presynaptic anatomical connections to the CPU injection site, provide a third basis for comparison with our hemogenetic functional connectivity results. Quantification of mCherry fluorescence levels across ROIs in four animals shows that the density of HSV-labeled cells in each ROI does not directly scale with the amplitudes of NOSTIC-dependent activity signals in the experiments of Fig. 3 (Fig. 5c). Mean NOSTIC and mCherry labeling signals are uncorrelated ($R = 0.37$, $P = 0.36$, $n = 8$ ROIs), and the ratio of labeled cell density to NOSTIC signal varies considerably among regions. SN shows the greatest viral labeling density of 92 ± 26 cells per mm^2 , significant above all ROIs except CPU and MCx (t -test $P \leq 0.027$, $n = 4$), but displays lower NOSTIC responses than several other areas. Although average labeled cell densities above 5 cells per mm^2 are observed in all regions with statistically significant NOSTIC signals, moderate retrograde viral labeling is also consistently observed in MT (6.7 ± 1.9 cells per mm^2 ; t -test $P = 0.039$, $n = 4$), a thalamic region in which LH stimulus-elicited NOSTIC signals are not pronounced. Our data thus demonstrate that connectivity strength judged using viral tract tracing does not predict functional responses measured using the hemogenetic imaging technique.

The combined brain-wide dataset consisting of circuit-specific hemogenetic readouts, nonspecific fMRI, resting state analysis and anatomical tracing of striatal afferents (Fig. 5d) yields an integrated view of neural information flow in and around the rodent striatum (Fig. 5e). The NOSTIC-1 results—confirmed by *c*-Fos histochemistry and calcium photometry—identify ECx, MCx and SN as distal input sources that shape striatal activity during stimulation, complementing local processing within CPU itself. Concurrent activation of cortical and midbrain afferents during LH-targeted DBS has not previously been documented, but might be important for behaviorally reinforcing properties of the stimulation^{29,30}. Meanwhile, CCx, ICx, MT and S1 are all strongly activated by LH stimulation and also correlated to CPU in the resting state, but these regions do not display statistically significant presynaptic input to CPU according to the NOSTIC-based fMRI measurements. A simple hypothesis to explain these results is that CCx, ICx, MT and S1 are excited by striatal outputs, but we cannot rule out the possibility that alternative conduction pathways are involved; further application of hemogenetic imaging could resolve this issue. Medial thalamic input to striatum is notably not observed, despite notable anatomical and resting state connectivity between MT and CPU and activation of MT by LH stimulation. These input/output relationships might collectively generalize to other experimental contexts, particularly those related to reward processing and motor control.

Discussion

The results we present here introduce and apply a sensitive strategy for brain-wide functional imaging of genetically targeted cells and neural projections. NOSTIC probes transduce intracellular calcium signaling into NO production, which in turn triggers hemodynamic responses that can be measured using fMRI and other neuroimaging modalities. Our studies demonstrate efficacy of the probes and their suitability for hemogenetic fMRI of neural populations labeled using a viral vector. ROI-level results are supported by established measures including activity-dependent *c*-Fos expression mapping and fluorescence recordings. The differential measurement strategy

used in the current work provides readouts of both NOSTIC-specific and intrinsic stimulus-driven hemodynamic activity. By combining these measures with resting state fMRI and postmortem histological analysis, we define distinct relationships between function and anatomy in striatal circuitry during reward-related DBS.

The NOSTIC probes work by tapping into physiology that naturally relates neural activity to changes in blood flow. An advantage of this approach is that it exploits intrinsic biological amplification mechanisms to detect the function of even relatively sparse cell populations. That said, hemogenetic imaging will need to be further benchmarked against conventional measurements of neural activity to determine its sensitivity characteristics more thoroughly. It is likely that comparisons of intracellular calcium dynamics with NOSTIC signals over a range of activity levels and labeled cell densities will expose nonlinearities that are characteristic of neurovascular coupling³¹. Such studies might also indicate whether perturbations are caused by the NOSTICs themselves, due to effects of excess NO production on neurophysiology or vascular biology³². Side-effects could be mitigated if needed by inducing probe expression only when needed, or by inhibiting it before imaging experiments. An additional source of complexity could arise from uncertainty as to how exactly NO causes vasodilation; both direct vasodilatory and indirect effects of neuronal NO on the vasculature have been proposed, and astrocytes and endothelial cells may help mediate the action of neurogenic NO on vessels^{33,34}. Such intricacies might particularly influence the performance of hemogenetic imaging in disease conditions where vascular status is altered or inflammatory NO production is a factor³⁵. Comparison of NOSTIC-dependent results with control conditions and additional tests to rule out confounds will continue to be important as bases for rigorous experimentation using the hemogenetic approach.

Despite current limitations of the technology, our analysis of striatal functional connectivity using the NOSTIC-1 activity reporter offers broader importance in several respects. First, this study demonstrates the complexity of responses to DBS. Although the LH stimulation we used is targeted at fibers that directly connect mid-brain nuclei to CPU, our results demonstrate engagement of neural pathways that extend far beyond these structures. The activation of distal CPU afferents from cortex we observe could not be anticipated based on anatomical considerations alone, and yet might be critical for behavioral outcomes of the stimulation paradigm. Our data thus imply that both direct effects and broader circuit-level consequences of targeted stimulation are important in determining how DBS affects the brain. Results from the DBS paradigm are also relevant to striatal function more generally, although the stimulus we used may induce unphysiological patterns of signal propagation or neurochemical release that differentiate our experiments from more naturalistic scenarios³⁶.

Second, our results indicate limitations of conventional approaches for understanding brain-wide connectivity. Anatomical tracing fails to predict which presynaptic inputs to the striatum are most relevant to the stimulus paradigm we explored, and conventional fMRI assessments during stimulation and resting states likewise fail to highlight circuit-specific functional relationships identified by the hemogenetic imaging approach. NOSTIC-based imaging thus provides information that is difficult to obtain using other neural readouts, including the combination of fMRI with cellularly targeted stimuli such as optogenetic manipulations^{37,38}. Although information about the activity of specific neuronal projections can be obtained using optical tagging³⁹ or genetically targeted fluorescent readouts such as the photometry we present in Fig. 4g–i, these approaches are technically challenging and difficult to apply over many brain regions in mammals. Meanwhile, methods such as the combined anatomical tracing and *c*-Fos histology we used for validation, as well as some forms of manganese-enhanced MRI⁴⁰, can also combine sensitivity to anatomical and functional

brain parameters, but they are not well-suited for monitoring activity dynamically on behaviorally relevant time scales.

Finally, the molecular neuroimaging strategy we used could be extended to many other experimental contexts. In the future, hemogenetic techniques could be applied in sedated or awake animals of many species, using virtually any wide-field imaging modality, and in conjunction with spatial or genetic targeting methods. Although we used an artificial stimulus to induce neural activity in our experiments, hemogenetic imaging may be compatible with more ecologically relevant stimuli or behavioral settings as well. As an alternative to hemodynamic imaging readouts, detection of NOSTIC probes could potentially be performed using molecular imaging strategies capable of directly measuring biogenic NO production *in vivo*^{41–43}. The invasive viral injection methods employed here could be avoided if noninvasive viral delivery^{44–46} or other transgenesis techniques prove feasible. Further efforts are required to evaluate probe performance across cell types, but our current results already demonstrate NOSTIC functionality in neural and non-neural cells and over multiple brain regions containing disparate cell populations; they even suggest the possibility of targeting the probes with subcellular precision using protein moieties such as the PDZ domain of NOSTIC-1P.

Targeted applications of NOSTICs might be particularly powerful for analyzing the basis of functional selectivity in high-level sensory processing, or for characterizing the roles of distinct cell types and projections in neural mechanisms of behavior. Further protein engineering could produce probes that operate with improved signal-to-noise ratio and under conditions where endogenous hemodynamics are suppressed⁴⁷. This would allow identification of NOSTIC-dependent signals without the subtractive imaging approach of Fig. 3, which in turn would improve the reliability of hemogenetic signal detection, particularly at single-animal and single-voxel levels. Protein engineering might also yield NOSTICs suitable for multiplexed measurements from more than one cell population in the same animal. Variants of our initial probes could be used to study processes such as neuroplasticity, neurochemical signaling and neurovascular coupling or the biology of NO itself. Hemogenetic technology thus offers a general strategy for mechanistic dissection of neural function on a brain-wide scale.

Online content

Any methods, additional references, Nature Research reporting summaries, source data, extended data, supplementary information, acknowledgements, peer review information; details of author contributions and competing interests; and statements of data and code availability are available at <https://doi.org/10.1038/s41593-022-01014-8>.

Received: 25 March 2020; Accepted: 14 January 2022;

Published online: 3 March 2022

References

- Nakai, J., Ohkura, M. & Imoto, K. A high signal-to-noise Ca²⁺ probe composed of a single green fluorescent protein. *Nat. Biotechnol.* **19**, 137–141 (2001).
- Belliveau, J. W. et al. Functional mapping of the human visual cortex by magnetic resonance imaging. *Science* **254**, 716–719 (1991).
- Ogawa, S. et al. Intrinsic signal changes accompanying sensory stimulation: functional brain mapping with magnetic resonance imaging. *Proc. Natl. Acad. Sci. USA* **89**, 5951–5955 (1992).
- Hu, S., Maslov, K., Tsytsarev, V. & Wang, L. V. Functional transcranial brain imaging by optical-resolution photoacoustic microscopy. *J. Biomed. Opt.* **14**, 040503 (2009).
- Mace, E. et al. Functional ultrasound imaging of the brain. *Nat. Methods* **8**, 662–664 (2011).
- Logothetis, N. K. The underpinnings of the BOLD functional magnetic resonance imaging signal. *J. Neurosci.* **23**, 3963–3971 (2003).
- Attwell, D. et al. Glial and neuronal control of brain blood flow. *Nature* **468**, 232–243 (2010).
- Krawchuk, M. B., Ruff, C. F., Yang, X., Ross, S. E. & Vazquez, A. L. Optogenetic assessment of VIP, PV, SOM and NOS inhibitory neuron activity and cerebral blood flow regulation in mouse somato-sensory cortex. *J. Cereb. Blood Flow. Metab.* **40**, 1427–1440 (2020).
- Burke, M. & Buhrlé, C. BOLD response during uncoupling of neuronal activity and CBF. *Neuroimage* **32**, 1–8 (2006).
- Stefanovic, B., Schwindt, W., Hoehn, M. & Silva, A. C. Functional uncoupling of hemodynamic from neuronal response by inhibition of neuronal nitric oxide synthase. *J. Cereb. Blood Flow. Metab.* **27**, 741–754 (2007).
- Zhou, L. & Zhu, D. Y. Neuronal nitric oxide synthase: structure, subcellular localization, regulation, and clinical implications. *Nitric Oxide* **20**, 223–230 (2009).
- Lee, S. J. & Stull, J. T. Calmodulin-dependent regulation of inducible and neuronal nitric-oxide synthase. *J. Biol. Chem.* **273**, 27430–27437 (1998).
- Brennan, J. E. et al. Interaction of nitric oxide synthase with the postsynaptic density protein PSD-95 and α 1-syntrophin mediated by PDZ domains. *Cell* **84**, 757–767 (1996).
- Schmidt, K. et al. Comparison of neuronal and endothelial isoforms of nitric oxide synthase in stably transfected HEK 293 cells. *Am. J. Physiol. Heart Circ. Physiol.* **281**, H2053–H2061 (2001).
- Shi, Z. et al. High spatial correspondence at a columnar level between activation and resting state fMRI signals and local field potentials. *Proc. Natl. Acad. Sci. USA* **114**, 5253–5258 (2017).
- Oh, S. W. et al. A mesoscale connectome of the mouse brain. *Nature* **508**, 207–214 (2014).
- Guo, Q. et al. Whole-brain mapping of inputs to projection neurons and cholinergic interneurons in the dorsal striatum. *PLoS ONE* **10**, e0123381 (2015).
- Hunnicutt, B. J. et al. A comprehensive excitatory input map of the striatum reveals novel functional organization. *eLife* **5**, e19103 (2016).
- Mandelbaum, G. et al. Distinct cortical-thalamic-striatal circuits through the parafascicular nucleus. *Neuron* **102**, 636–652 e637 (2019).
- Stuber, G. D. & Wise, R. A. Lateral hypothalamic circuits for feeding and reward. *Nat. Neurosci.* **19**, 198–205 (2016).
- Schlaepfer, T. E., Bewernick, B. H., Kayser, S., Madler, B. & Coenen, V. A. Rapid effects of deep brain stimulation for treatment-resistant major depression. *Biol. Psychiatry* **73**, 1204–1212 (2013).
- Whiting, D. M. et al. Lateral hypothalamic area deep brain stimulation for refractory obesity: a pilot study with preliminary data on safety, body weight, and energy metabolism. *J. Neurosurg.* **119**, 56–63 (2013).
- Moisan, J. & Rompre, P. P. Electrophysiological evidence that a subset of midbrain dopamine neurons integrate the reward signal induced by electrical stimulation of the posterior mesencephalon. *Brain Res.* **786**, 143–152 (1998).
- Fenno, L. E. et al. Targeting cells with single vectors using multiple-feature Boolean logic. *Nat. Methods* **11**, 763–772 (2014).
- Li, N. & Jasanoff, A. Local and global consequences of reward-evoked striatal dopamine release. *Nature* **580**, 239–244 (2020).
- Okada, S. et al. Calcium-dependent molecular fMRI using a magnetic nanosensor. *Nat. Nanotechnol.* **13**, 473–477 (2018).
- Park, Y. G. et al. Protection of tissue physicochemical properties using polyfunctional crosslinkers. *Nat. Biotechnol.* **37**, 73–83 (2018).
- Biswal, B., Yetkin, F. Z., Haughton, V. M. & Hyde, J. S. Functional connectivity in the motor cortex of resting human brain using echo-planar MRI. *Magn. Reson. Med.* **34**, 537–541 (1995).
- Adamantidis, A. R. et al. Optogenetic interrogation of dopaminergic modulation of the multiple phases of reward-seeking behavior. *J. Neurosci.* **31**, 10829–10835 (2011).
- Bamford, N. S., Wightman, R. M. & Sulzer, D. Dopamine's effects on corticostriatal synapses during reward-based behaviors. *Neuron* **97**, 494–510 (2018).
- Buxton, R. B., Uludag, K., Dubowitz, D. J. & Liu, T. T. Modeling the hemodynamic response to brain activation. *Neuroimage* **23**, S220–S233 (2004).
- Picon-Pages, P., Garcia-Buendia, J. & Munoz, F. J. Functions and dysfunctions of nitric oxide in brain. *Biochim. Biophys. Acta Mol. Basis Dis.* **1865**, 1949–1967 (2019).
- Hillman, E. M. Coupling mechanism and significance of the BOLD signal: a status report. *Annu. Rev. Neurosci.* **37**, 161–181 (2014).
- Nippert, A. R., Biesecker, K. R. & Newman, E. A. Mechanisms mediating functional hyperemia in the brain. *Neuroscientist* **24**, 73–83 (2018).
- D'Esposito, M., Deouell, L. Y. & Gazzaley, A. Alterations in the BOLD fMRI signal with ageing and disease: a challenge for neuroimaging. *Nat. Rev. Neurosci.* **4**, 863–872 (2003).
- Jakobs, M., Fomenko, A., Lozano, A. M. & Kiening, K. L. Cellular, molecular, and clinical mechanisms of action of deep brain stimulation—a systematic review on established indications and outlook on future developments. *EMBO Mol. Med.* **11**, e9575 (2019).
- Lee, J. H. et al. Global and local fMRI signals driven by neurons defined optogenetically by type and wiring. *Nature* **465**, 788–792 (2010).

38. Desai, M. et al. Mapping brain networks in awake mice using combined optical neural control and fMRI. *J. Neurophysiol.* **105**, 1393–1405 (2011).
 39. Lima, S. Q., Hromadka, T., Znamenskiy, P. & Zador, A. M. PINP: a new method of tagging neuronal populations for identification during in vivo electrophysiological recording. *PLoS ONE* **4**, e6099 (2009).
 40. Pautler, R. G. & Koretsky, A. P. Tracing odor-induced activation in the olfactory bulbs of mice using manganese-enhanced magnetic resonance imaging. *Neuroimage* **16**, 441–448 (2002).
 41. Yoshimura, T. et al. In vivo EPR detection and imaging of endogenous nitric oxide in lipopolysaccharide-treated mice. *Nat. Biotechnol.* **14**, 992–994 (1996).
 42. Reinhardt, C. J., Zhou, E. Y., Jorgensen, M. D., Partipilo, G. & Chan, J. A ratiometric acoustogenic probe for in vivo imaging of endogenous nitric oxide. *J. Am. Chem. Soc.* **140**, 1011–1018 (2018).
 43. Barandov, A. et al. Molecular magnetic resonance imaging of nitric oxide in biological systems. *ACS Sens.* **5**, 1674–1682 (2020).
 44. Wang, S., Olumolade, O. O., Sun, T., Samiotaki, G. & Konofagou, E. E. Noninvasive, neuron-specific gene therapy can be facilitated by focused ultrasound and recombinant adeno-associated virus. *Gene Ther.* **22**, 104–110 (2015).
 45. Deverman, B. E. et al. Cre-dependent selection yields AAV variants for widespread gene transfer to the adult brain. *Nat. Biotechnol.* **34**, 204–209 (2016).
 46. Szablowski, J. O., Lee-Gosselin, A., Lue, B., Malounda, D. & Shapiro, M. G. Acoustically targeted chemogenetics for the non-invasive control of neural circuits. *Nat. Biomed. Eng.* **2**, 475–484 (2018).
 47. Leithner, C. et al. Pharmacological uncoupling of activation induced increases in CBF and CMRO₂. *J. Cereb. Blood Flow Metab.* **30**, 311–322 (2010).
- Publisher's note** Springer Nature remains neutral with regard to jurisdictional claims in published maps and institutional affiliations.
- © The Author(s), under exclusive licence to Springer Nature America, Inc. 2022

Methods

Animal subjects. Adult male Sprague-Dawley rats (200–250 g, 7–8 weeks old) were purchased from Charles River Laboratories. After arrival, animals were housed and maintained on a 12-h light/dark cycle and permitted ad libitum access to food and water. All procedures were carried out in strict compliance with National Institutes of Health guidelines, under oversight of the Committee on Animal Care at the Massachusetts Institute of Technology as part of protocol number 0721-059-24.

Statistics and reproducibility. Experiments were performed on multiple samples or animals to ensure reproducibility and permit group-level comparisons. Relevant statistics are reported throughout the text. Data distributions were assumed to be normal but were not formally tested. All statistical results were evaluated with two-sided significance criteria. No statistical method was used to predetermine sample size. Data from major technical failures (for example, damaged tissue, poor image quality) were excluded from analysis. Randomized allocation was not performed, and investigators were not blinded to allocation during experiments and outcome assessment.

Construction of engineered NOS variants. The plasmid pCWori containing human iNOS and rat nNOS constructs were a generous gift from the laboratory of Dr. Thomas Poulos at the University of California, Irvine. The nNOS and iNOS were individually cloned into the pIRESpuro3 mammalian vector (Takara Bio USA). An inverse PCR was performed to create the backbone. Inserts were amplified from the pCWori backbone using overhangs ranging from 24 to 30 nucleotides on each end. A single-step, isothermal, ligation-free procedure was used to integrate the inserts. The entire length of the coding strand was verified using sequencing. A similar DNA assembly strategy was used to generate chimeric genes encoding NOSTIC-1 and NOSTIC-1P. Sequences of the chimeric proteins are provided in Supplementary Table 1.

The following strategy was used to build genetic constructs for making stable cell lines: A lentiviral backbone containing the cytomegalovirus promoter driving enhanced GFP (eGFP) with a blasticidin resistance cassette driven by a phosphoglycerate kinase promoter (pLV6-eGFP-BLA) was used to generate pLV6-NOSTIC-1-BLA. The parent plasmid was treated with BamHI (NEB) and EcoRI (NEB) to make linearized vector. NOSTIC-1 was amplified using PCR with primers having 20–25-base-pair overhang. The purified PCR product and the linearized backbone were assembled using Gibson assembly (NEB). DNA was transformed into Stable competent cells (NEB). The entire coding strand was verified by Sanger sequencing (Quintara Biosciences).

Expression and activity of NOS clones in cell culture. FreeStyle 293-F cells were obtained from Thermo Fisher and maintained according to the supplier's protocol. To test for expression and activity of NOS constructs expressed in these cells, high-purity DNA suitable for transfection was obtained using the Qiagen Plasmid Maxi Kit. DNA was introduced into the cells using 293Fectin (Thermo Fisher) following the manufacturer's protocols. At 48 h post-transfection, cells were pelleted and resuspended in Freestyle 293 Expression Medium (Thermo Fisher) containing 1 mM L-arginine and 1 mM CaCl₂ and seeded in six-well plates at 2 million cells per well. Cells were stimulated with 5 μM A23187 (MilliporeSigma). Catalytic activity of NOS constructs was determined by quantifying nitrite from the supernatant using the Griess test (Promega). Assays were performed in multiwell plates and results read spectrophotometrically using a Molecular Devices plate reader operated using the manufacturer-supplied SoftMax Pro software. For experiments to test for inhibitor sensitivity of different NOS constructs, L-nitroarginine methyl ester (L-NAME) hydrochloride and 1400W were purchased from MilliporeSigma and added to resuspension medium before stimulation of the cells.

293FT cells (Thermo Fisher) were used to generate stable lines and were maintained in accordance with the manufacturer's guidelines. Cells were cotransfected with either pLV6-NOSTIC-1-BLA or pLV6-eGFP along with plasmids pSPAX2 and pMD2.G (Addgene) using Lipofectamine 3000 (Thermo Fisher). At 48 h post-transfection the supernatant containing lentiviral particles was added to freshly seeded cells on a 10-cm tissue culture dish. At 24 h following the addition of the lentiviral supernatant, the medium was aspirated and changed to fresh DMEM with 10% FBS (Thermo Fisher) containing 10 μg ml⁻¹ blasticidin. Medium was changed every 48 h until the dish was about 80% confluent.

Catalytic activity of the stably expressing NOSTIC cell line was tested using the Griess test after stimulation with A23187 as described above. To test for expression of NOSTIC, cells stably expressing either eGFP or NOSTIC-1 were seeded on poly-D-lysine-coated coverslips (Thermo Fisher). When these cells were about 60% confluent, they were fixed with 4% paraformaldehyde (PFA) for 15 min, rinsed thrice with PBS, permeabilized with buffer containing PBS and 3% Triton X (MilliporeSigma) for 15 min, and blocked with buffer containing PBS and 10% donkey serum (MilliporeSigma) for 60 min. The cells were then incubated with primary antibody (goat anti-nNOS, Abcam) at 1:200 dilution at 4 °C. Following overnight incubation, cells were rinsed thrice with PBS and incubated with secondary antibody (donkey anti-goat IgG, tagged with Alexa Fluor 488, Thermo Fisher) at 1:500 dilution for 1 h. The coverslips were rinsed thrice and mounted on glass slides with ProLong Antifade Mountant (Thermo Fisher). These were then

imaged on a confocal microscope (LSM 710, Carl Zeiss), controlled with Zeiss ZEN software.

To examine NOSTIC-mediated NO production in central nervous system-derived cells, NOSTIC and control clones were expressed in CAD cells, a subclone of the catecholergic rat Cath.a neuronal tumor line⁴⁸. These cells were maintained in 1:1 DMEM/Ham's F12 nutrient mixture plus 10% FBS (Thermo Fisher). To test for catalytic activity, NOSTIC-1 fused to mCherry (NOSTIC-mCherry) or mCherry alone (control) was transfected using Lipofectamine 3000. The next day, cells were incubated with 5 μM A23187 and 100 μM 1400W (where indicated) in reduced serum Opti-MEM medium (Thermo Fisher). Nitrite was quantified using the Griess test. To obtain micrographs, CAD cells were seeded on poly-D-lysine coverslips and transfected with NOSTIC-mCherry or mCherry. The following day, cells were incubated with 2 μM DAF (4-amino-5-methylamino-2',7'-difluorescein, diamino fluorescein-FM) in Tyrode solution (VWR) and stimulated with 5 μM A23187 in the presence or absence of 100 μM 1400W, as indicated. The cells were fixed in 4% PFA in PBS and washed thrice before imaging.

Brain implantation of NOSTIC-expressing cells. 293FT cells stably expressing NOSTIC-1 or GFP were collected by trypsinization, pelleted by centrifugation for 10 min at 300g, washed with cold PBS (pH 7.4) and resuspended at a density of 100,000 cells per μl in artificial cerebrospinal fluid (125 mM NaCl, 2.5 mM KCl, 1.4 mM CaCl₂, 1 mM MgCl₂, 1.25 mM NaH₂PO₄, 25 mM NaHCO₃).

Before intracranial cell implantation in rats, each animal was anesthetized with isoflurane (4% for induction, 2% for maintenance) and positioned in a stereotaxic instrument (Kopf Instruments) with a water heating pad (Braintree Scientific) to keep the body temperature at 37 °C. The scalp was surgically retracted and two small holes were drilled into the skull above the target sites 0.5 mm posterior and ±3 mm lateral to bregma. 28 G polyether ether ketone (PEEK) cannula guides (Plastics One) designed to project 1 mm below the surface of the skull were lowered through the holes. The guides were fixed in place using SEcure light-curing dental cement (Parkell). A custom-fabricated plastic headpost was placed in front of the guide cannula and also secured with dental cement (Parkell).

To deliver cells, 33 G metal internal cannulae (Plastics One) were lowered through the guide cannulae to a depth of 5.5 mm below the skull. Approximately 500,000 NOSTIC-expressing or control cells were infused via the cannulae at a flow rate of 0.2 μl min⁻¹ for 25 min, with test and control sites alternating among experiments to negate potential biases. At 10 min after the infusion the cannulae were slowly removed.

MRI of implanted cells in vivo. After implantation of NOSTIC-expressing or control GFP-expressing cells, the metal cannulae were removed. Animals were intubated and ventilated with a small animal ventilator (Harvard Apparatus) which operated at 62 beats per minute with a 6-ml stroke volume, delivering oxygen and air as a 5:1 ratio mixture. Each animal was then transferred and fixed into a custom rat imaging cradle. A surface receive-only radiofrequency coil (Doty Scientific) was positioned over the head. 33 G PEEK internal cannulae (Plastics One) were connected to PE-50 tubing (Plastics One) loaded with the calcium ionophore A23187 (10 μM), with or without the NOSTIC-1 inhibitor 1400W (100 μM), and lowered through the guide cannulae to the same site for cells implantation, at a depth of 5.5 mm below the skull. Isoflurane was discontinued and the animal was sedated with medetomidine (intraperitoneal (i.p.) bolus of 0.1 mg kg⁻¹, followed by 0.1 mg kg⁻¹ h⁻¹ infusion) and paralyzed with pancuronium (i.p. bolus of 1 mg kg⁻¹, followed by 1 mg kg⁻¹ h⁻¹ infusion). Each animal was then transferred to a 9.4 T Bruker MRI scanner for imaging. Animals were warmed using a water heating pad (Braintree). Heart rate and blood oxygenation saturation level were continuously monitored using an MRI-compatible infrared pulse oximeter (Nonin Medical). Breathing rate and CO₂ level were continuously monitored using an MRI-compatible SurgiVet CO₂ monitor (Smiths Medical).

All MRI images were obtained using a transmit-only 70-cm-inner-diameter linear volume coil (Bruker) and a 2-cm-diameter receive-only surface coil (Doty) for excitation and detection, respectively. Scanner operation was controlled using the ParaVision 5.1 software (Bruker). Fieldmap shimming was performed to optimize main field (B₀) homogeneity. High-resolution anatomical MRI images were acquired using a longitudinal relaxation time (T₂)-weighted rapid acquisition with refocused echoes (RARE) pulse sequence with RARE factor = 8, bandwidth = 200 kHz, effective echo time (TE) = 30 ms, repetition time (TR) = 5 s, in-plane field of view (FOV) = 2.56 × 1.28 cm², in-plane resolution of 100 × 100 μm² and slice thickness = 1 mm. Functional imaging scan series were acquired using a multi-echo echo-planar imaging (EPI) pulse sequence with TE values = 10, 23 and 36 ms; flip angle = 90°, TR = 2 s, FOV = 2.56 × 1.28 cm² and in-plane resolution of 400 × 400 μm² over five coronal slices with slice thickness = 1 mm.

MRI scans were continuously collected for 2 min of baseline, for 5 min during calcium stimulation or control treatment, and for 10 min of resting after the stimulation. Calcium stimulation was produced by infusion of a 10 μM solution of A23187 in artificial cerebrospinal fluid, at a rate of 0.2 μl min⁻¹ through the preimplanted plastic cannulae. Control treatment involved infusion of an identical solution that also contained 100 μM 1400W. Effective T₂ (T₂^{*})-dependent contributions to the functional imaging data were extracted from the multi-echo

image time series by examining data at three echo times, permitting voxels with strong TE dependence characteristic of BOLD contrast to be identified⁴⁹. T_2^* -weighted signal was defined as an average of signals observed at each echo time, weighted by TE , while non- T_2^* -dependent signal components, largely along the cell implantation tracks, were rejected.

The preprocessed data were then further analyzed in MATLAB (MathWorks) for visualization and quantification of results. Response maps were computed as mean percent signal change during the expected peak response time point 1–100 s after A23187 stimulation onset minus the average baseline signal, 1–100 s before stimulus onset. Mean response amplitudes and time courses were evaluated over an ROI defined around each cell implantation site. These ROIs were defined by the edges of the implanted xenografts, as judged from the high-resolution T_2 -weighted anatomical scans, expanded by four voxels in each in-plane direction.

Preparation of herpes simplex viral vectors. Herpes simplex virus (HSV) type 1 vectors used in this study were produced by Rachael Neve at the Massachusetts General Hospital Gene Delivery Technology Core. The vectors are replication deficient and capable of retrograde transport from injection sites in rodent brain. NOSTIC-1 expression was directed by an HSV containing the NOSTIC-1 gene in tandem with the gene for mCherry, separated by an internal ribosome entry site (IRES), with expression directed by the human EF1 α promoter (HSV-hEF1 α -NOSTIC-1-IRES-mCherry). A control vector directed expression of mCherry only from the same promoter (HSV-hEF1 α -mCherry).

Virally delivered NOSTIC-1 was tested for catalytic activity in cell culture. Approximately 200,000 HEK293FT (Thermo Fisher) cells were seeded on poly-D-lysine- and laminin-coated coverslips (Thermo Fisher) in a 24-well plate. The following day, 1 μ l of 10^9 plaque-forming units (p.f.u.) ml⁻¹ HSV delivering NOSTIC-1 or mCherry was added to each well. At 24–48 h later, media was aspirated, washed, and the cells were stimulated with 5 μ M A23187 in 400 μ l of FreeStyle 293 Expression medium (Thermo Fisher) per well, supplemented with 1 mM CaCl₂. Nitrite was quantified from supernatants using the Griess assay following overnight incubation.

Stereotaxic injection of viral vectors. Animals were prepared for cranial surgery to expose the desired viral injection site at the anterior central CPU. Each animal was anesthetized with isoflurane (4% for induction, 2% for maintenance). A small hole was drilled into the skull above the target site, 0.5 mm posterior and 3 mm lateral to bregma. 35 G metal internal canulae connected with Hamilton syringes preloaded with each viral vector (NOSTIC-1: 1×10^9 p.f.u. ml⁻¹, mCherry: 2×10^9 p.f.u. ml⁻¹) were then lowered into the brain and each vector was infused at a rate of 0.1 μ l min⁻¹ at two sites (3 μ l per site), 6 mm and 5 mm below the skull surface. The canulae were slowly removed 10 min after the viral injection. Bone wax was applied to each injection site to seal it using a sterile cotton applicator tip. Skin incisions were closed by sterile wound clips and lidocaine gel (2%) was applied over the wound areas. Isoflurane was then discontinued and each rat was removed from the stereotaxic frame and placed in a warmed cage on a heating pad to recover for 45 min. Slow-release buprenorphine (0.3 mg kg⁻¹, MIT Pharmacy) was administered subcutaneously to minimize pain and discomfort. Wound clips were removed 7–10 d after surgery and when the wounds had healed.

Implantation of stimulation electrodes. Three weeks after viral injection, rats underwent a second surgery to implant electrodes suitable for DBS of the medial forebrain bundle region of the LH. Animals were prepared similarly for cranial surgery to expose the desired stimulation site. Bipolar stimulating electrodes were targeted to coordinates 3.4 mm posterior, 1.7 mm medial and 8.6 mm ventral to bregma. In addition, a plastic headpost was placed to facilitate positioning of each animal during MRI scanning. After all the items were secured on the skull, dental cement was applied to the entire exposed skull surface area to hold them rigidly in place. After the surgery, animals were maintained under a heating pad and treated with 0.3 mg kg⁻¹ slow-release buprenorphine subcutaneously during a convalescence period. Rats were allowed 4–7 d for recovery before fMRI experiments.

fMRI. Preparation of animals for fMRI was similar to that described above for xenograft implantation experiments. After intubation via a tracheotomy and ventilation, each animal was transferred to the MRI cradle and fixed by the headpost. For imaging of rats during LH stimulation, each animal's LH electrode was connected to a constant-current stimulus isolator (World Precision Instruments) controlled from a laptop computer. For imaging of rats during somatosensory stimulation, each animal was implanted with subcutaneous electrodes in the forelimb, which were similarly connected to the stimulus isolator.

General MRI methods, including hardware and anatomical imaging, were similar to those described above for xenograft-implanted animals. Functional imaging of HSV-transfected rats included 2 min of baseline image acquisition followed by five cycles of electrical stimulation, each consisting of 16 s of LH stimulation followed by 5 min of rest. Each 16-s stimulation block consisted of eight 1-s trains of 1-ms, 0.17-mA current pulses delivered at a frequency of 60 Hz, separated by 1 s between trains. Functional imaging with forepaw stimulation consisted of six blocks of 3-mA, 1-ms pulses repeated at 9 Hz for 10 s alternating

with 40 s of rest for tests evaluating effects of 1400W, and 20 s alternating with 80 s of rest for tests evaluating effects of L-NAME. In each case, the stimulation paradigm was synchronized with the image acquisition using a custom script executed in LabVIEW (National Instruments). To minimize potential radiofrequency artifacts, the stimulator cable was filtered with a 60-MHz low-pass filter (Mini-Circuits) before entering the MRI enclosure.

A T_2^* -weighted EPI sequence was used for detection of stimulus-induced BOLD contrast, with bandwidth = 200 kHz, a single TE of 16 ms, flip angle = 90°, $TR = 2$ s, $FOV = 2.56 \times 1.28$ cm², in-plane resolution of 400×400 μ m² and 12 slices with slice thickness = 1 mm. To discern NOS inhibitor dependence of forepaw stimulus-induced fMRI signals, image series from each animal were acquired first in the absence and then in the presence of systemically delivered 1400W (25 mg kg⁻¹ intravenously) or L-NAME (50 mg kg⁻¹ intravenously). For homogenetic experiments, identical procedures were applied using animals infected with NOSTIC-encoding and control viruses.

Analysis of functional imaging data. Images were reconstructed using the ParaVision 5.1 software and then imported into the National Institute of Health AFNI software package⁵⁰ for further processing. High-resolution anatomical images of each animal were registered to a Waxholm coordinate space rat brain atlas⁵¹. Functional imaging time series were preprocessed in steps that included slice timing correction, motion correction using a least-squares rigid-body volume registration algorithm, voxelwise intensity normalization, spatial smoothing with Gaussian spatial kernel of 0.5-mm full-width at half-maximum and spatial resampling to double the image matrix size, all implemented in AFNI. Segmentation of brain from nonbrain voxels was performed in MATLAB. Preprocessed time series were then coregistered onto the previously atlas-aligned anatomical images. Slices at the rostral and caudal extents of the imaging volume had poor image or registration quality and were eliminated from further analysis; slices exhibiting substantial electrode artifacts were likewise omitted. ROIs used for subsequent analyses were also defined with respect to the rat atlas and are displayed in Supplementary Fig. 2.

For all functional imaging data, stimulus-dependent impulse response functions (IRFs) were estimated from T_2^* -weighted EPI time courses using the 3dDeconvolve general linear modeling implementation in AFNI. This analysis computes IRFs that vary independently across positions in the brain, and thus avoids artifacts that can arise in general linear modeling approaches that employ a single spatially invariant hemodynamic response function. To compute voxel-specific IRFs, LH stimulus time blocks were used as event regressors. Six motion correction parameters from each animal were included as nuisance regressors, along with a linear baseline term. IRFs of 242-s duration (121 image frames) were obtained in units of percent signal change for each voxel.

For homogenetic experiments, mean percent signal change maps were derived from IRFs computed at the group level, among HSV-NOSTIC ($n = 6$) or HSV-mCherry ($n = 5$) animals, separately in the absence and presence of 1400W. Response amplitudes were defined as the average IRF signal over 174 s (87 image frames) beginning at stimulus onset, minus the baseline signal defined by the mean of response at time points 0–40 s (20 frames) before stimulus onset. To correct for systematic changes in hemodynamic amplitudes between pre- and post-1400W conditions, fMRI responses obtained after 1400W treatment were renormalized so that the response amplitude along the midline (assumed to be NOSTIC-independent) matched that observed before 1400W treatment. Difference maps were then calculated by subtracting the mean response amplitude map with 1400W treatment from the corrected mean response amplitude map without 1400W treatment from the same set of animals. Results are presented for voxels that showed significant stimulus responses as defined by F -test results of $P \leq 0.01$ from the group regression analyses in the pre-1400W condition.

A second set of 1400W-dependent difference maps was computed using a different general linear modeling approach that assumes a fixed stimulus-associated IRF (that is, hemodynamic response) for each voxel in each animal. The CPU IRF computed from the analysis described above was used for this purpose. Input to the regression analysis consisted of group data from all animals imaged in both pre- and post-1400W experimental periods, normalized by midline responses as above, to account for signal drift. These data were subjected to a standard regression analysis that included regressors to account for intrinsic BOLD signal and NOSTIC-specific BOLD signal, and six motion correction parameters as nuisance regressors, along with a linear baseline term. The intrinsic BOLD regressor was computed by convolving all stimulus blocks with the CPU IRF, while the NOSTIC regressor was computed by convolving pre-1400W stimulus blocks only with the CPU IRF. Maps of regression coefficients (β values) for the NOSTIC-specific BOLD signal are presented in Supplementary Fig. 5.

ROI-specific response values were obtained by computing IRF amplitudes described above separately for every animal, thus accounting for interanimal variability, and then averaging each animal's IRFs over the corresponding anatomical regions defined in Supplementary Fig. 2. Similarly, ROI-specific time courses were obtained by averaging signal time courses over anatomically defined regions and then over animals. All voxels from each ROI were included in the calculations, independent of statistical thresholds. Statistical analysis of 1400W effects was performed using paired t -tests of differences in each ROI before

versus after drug treatment. Brain regions contralateral to the LH stimulation electrode were not analyzed in detail, although some 1400W-dependent differences and HSV-driven NOSTIC expression were observed in contralateral CPu and MCx, in particular. A dorsoventral region of the brain also displayed substantial 1400W-dependent modulation in one animal only and contributes to signal in the NOSTIC-1 difference map of Fig. 3c; this difference signal is not statistically significant (paired *t*-test $P=0.14$, $n=6$). Unless otherwise noted, error bars and error margins associated with ROI-specific results throughout the text denote s.e.m. over multiple animals.

For forepaw stimulation experiments of Fig. 1 and Extended Data Fig. 2, mean response amplitudes were determined as the average IRF signal over 6 s (three image frames) beginning after stimulus onset, minus the prestimulation baseline average. Difference maps of Fig. 1e were computed by subtracting the mean response map with 1400W or L-NAME treatment from the map without treatment from the same animals, and statistical evaluation of ROI-level effects was performed using paired *t*-tests of differences in the SIFL region before versus after drug treatment. For resting state connectivity analysis presented in Fig. 5 and Extended Data Fig. 10, mean signal time courses for each ROI were calculated from EPI image series acquired from four naïve rats in the absence of stimulation. The Pearson correlation coefficients and the corresponding Fisher-transformed *Z* values were computed between the time courses of the viral injection subregion of CPu (bregma -0.5 mm) and the eight ROIs. Student's *t*-tests were used to evaluate statistical significance of *Z* values and associated comparisons.

Photometry recordings. Six rats were injected with LT-HSV-GCaMP6s or LT-HSV-GFP viral vectors into the CPu, using methods analogous to injection of LT-HSV-NOSTIC-1 for hemogenetic fMRI experiments. Three weeks after viral injection, the animals were anesthetized with isoflurane (4% for induction, 2% for maintenance), fixed into a stereotaxic frame and implanted with an LH stimulation electrode. A multimodal optic fiber (200- μ m diameter, Thorlabs) was subsequently inserted into a craniotomy above SN (4.8 mm posterior, 2.0–2.5 mm lateral and 7.0 mm ventral to bregma) and held in place by the stereotaxic arm.

Fluorescence signals were recorded at different depths ranging from 7.0 to 8.5 mm ventral to bregma by lowering the fiber in 0.5-mm steps for each recording during LH stimulation delivered at 60 Hz for 1-s blocks every 10 s at 0.15-mA current. A commercially available setup (FOM-II, NPI Electronic) delivered light for excitation of the calcium indicator via a 650-mW light-emitting diode (LED) with a nominal peak wavelength of 470 nm. LED power was controlled by an adjustable current source. The light beam was focused using a fixed-focus collimator onto one end of the optic fiber, which was connected to the system using an SMA connector. An aspheric lens was used to guide emitted fluorescence back from the same fiber, where it was focused onto a silicon photomultiplier photodetector with an active area of 3×3 mm² and a photon detection efficiency of 20% at 490 nm. The recorded fluorescence signals were low-pass filtered at 50 Hz, amplified with a gain of 50 (LPBF-01GD, NPI Electronic) and digitized with a sampling frequency of 1 kHz using a multifunction data acquisition interface (Power1401, Cambridge Electronic Design) and its corresponding acquisition software (Spike2). Fluorescence signals were analyzed in MATLAB. All traces represent relative changes in fluorescence intensity ($\Delta F/F$) and were low-pass filtered at 10 Hz and smoothed using a running average of 0.5 s before being averaged over 40 stimulation trials each.

Brain clearing and imaging. Brain fixation and clearing was performed using a technique known as stabilization under harsh conditions via intramolecular epoxide linkages to prevent degradation (SHIELD)³⁷. Three weeks after the HSV-mCherry virus injection, rats were transcardially perfused with 200 ml of ice-cold PBS containing 0.02% sodium azide (PBSN), followed by 200 ml of ice-cold SHIELD perfusion solution at a flow rate of 60 ml min⁻¹. The brain was extracted and incubated in SHIELD perfusion solution at 4°C on an orbital shaker for 2 d. The brain was then moved to 50 ml of SHIELD OFF solution and incubated on an orbital shaker for 3 d at 4°C. After SHIELD OFF incubation, the brain was incubated in 40 ml of SHIELD ON solution that had been prewarmed at 37°C for 20 min. SHIELD ON incubation occurred on an orbital shaker at 37°C for 1 d. Following the completion of SHIELD processing, the brain was washed in PBSN for at least 1 d. SHIELD processing solutions were obtained from LifeCanvas Technologies.

The brain was hemisected after washing. The meninges surrounding the brain were then stained using a solution of 1% toluidine blue in 70% ethanol, diluted tenfold in PBSN. The brain was briefly immersed in the staining solution and then placed under a stereoscope equipped with a fiber-optical illuminator. A blunt-tipped paint brush was used to separate the dura layer from the surface of the brain. Hemispheres were then passively incubated for 48 h at room temperature in a tissue clearing buffer containing SDS. After incubation, intact hemispheres were rapidly delipidated via stochastic electrotransport at 45°C for 10–14 d (ref. 52). Optical clearing proceeded until the core of each sample showed no signs of opacity. Samples were then rinsed in PBSN three times for a minimum of 12 h each. Before volumetric labeling, samples were passively incubated for 48 h at room temperature in eFLASH sample buffer⁵³. Rapid 24-h immunostaining of whole hemispheres with polyclonal CF640R rabbit anti-RFP (Biotium) was carried out

using the eFLASH protocol⁵³. The samples were again passively washed in PBSN three times for a minimum of 12 h each before refractive index matching.

After clearing and labeling, the intact rat hemisphere was optically cleared using a Protos-based immersion medium. The tissue was incubated for 2 d at 37°C until tissue was transparent. Once optically cleared, the tissue was mounted in an agarose block (1.5% wt/vol agarose powder dissolved in immersion medium) and volumetrically imaged with an axially swept lightsheet microscope (LifeCanvas Technologies) using a custom $\times 3.6$ -magnification, 0.2-numerical-aperture detection objective with a uniform axial resolution of approximately 4 μ m. This system is equipped with an Oxixius L4Cc laser combiner unit equipped with 488-nm, 561-nm, 642-nm and 785-nm diodes; anti-RFP images were acquired using the 642-nm unit. The 900-GB raw lightsheet dataset was stitched into a single 92-GB Imaris (Bitplane) dataset for visualization.

Conventional immunohistochemical analysis. For immunohistochemistry analysis of activity-dependent gene induction in conjunction with other markers, rats injected with HSV-hEF1a-NOSTIC-1-IRES-mCherry were anesthetized via an i.p. injection of a ketamine (90 mg kg⁻¹) and xylazine (10 mg kg⁻¹) mixture. At 30 min after the induction of anesthesia, the rats were subjected to a sequence of five trials of LH stimulation using the same stimulation parameters as in the fMRI experiments, with 1-min rests between trials. Rats were then transferred back to their own cage for 90 min to allow for *c*-Fos expression and accumulation before the animals were killed by lethal i.p. injection of a sodium pentobarbital (0.5 mg g⁻¹ Fatal-Plus), in conjunction with transcardial perfusion with 4% PFA.

Brains were collected and fixed in PFA for an additional 48 h at 4°C. Extracted brains were then sectioned into 50- μ m-thick free-floating coronal slices using a semiautomatic vibratome (VT1200, Leica Biosystems). Slices were stored in PBS at 4°C. Before staining, slices were washed thrice in PBS + 0.1% TritonX (PBST) and blocked for 1 h with 10% v/v donkey serum (MilliporeSigma). Each slice was then incubated overnight at 4°C with gentle shaking in PBST with 1% serum and primary antibody. The following primary antibodies were used: goat anti-mCherry (1:200, Lifespan Biosciences), rabbit anti-mCherry (1:200, Abcam), rabbit anti-*c*-Fos (1:500, Synaptic Systems), goat anti-IBA-1 (1:500, Abcam), rabbit anti-nitrotyrosine (1:200, MilliporeSigma).

The following day, tissue was washed thrice with PBST and then probed with secondary antibody (Thermo Fisher or Abcam). The following secondary antibodies were used: donkey anti-rabbit IgG tagged with Alexa Fluor 594, donkey anti-goat IgG tagged with Alexa Fluor 488, donkey anti-goat IgG tagged with Alexa Fluor 594 or donkey anti-rabbit IgG tagged with Alexa Fluor 488, all applied in PBST with 1% serum for 1 h. Slices were then washed thrice in PBS, mounted on glass slides using Prolong Antifade Mountant with DAPI (Thermo Fisher) and imaged on a confocal microscope (LSM 710, Carl Zeiss).

To perform quantitative analysis of immediate early gene activation, ImageJ (National Institutes of Health) was used to quantify the total number of *c*-Fos- or mCherry-expressing cells by counting all cells exhibiting homogenous fluorescence at noticeably higher levels than the background fluorescence in the images, which was kept constant throughout the counting process for all images. Counting regions were defined by overlaying brain atlas sections⁵⁴ on the histological images based on landmarks for the relevant brain areas, and cells were distinguished by both color and distribution of fluorescence. Cells expressing both *c*-Fos and mCherry markers were identified by overlap of morphological features in the green and red channels of each image.

Reporting Summary. Further information on research design is available in the Nature Research Reporting Summary linked to this article.

Data availability

Source data for Figs. 1–5 and the associated Extended Data figures are provided with this paper.

Code availability

Processing scripts used in the data analysis are available from the corresponding author on request.

References

- Qi, Y., Wang, J. K. T., McMillan, M. & Chikaraishi, D. M. Characterization of a CNS cell line, CAD, in which morphological differentiation is initiated by serum deprivation. *J. Neurosci.* **17**, 1217–1225 (1997).
- Kundu, P., Inati, S. J., Evans, J. W., Luh, W. M. & Bandettini, P. A. Differentiating BOLD and non-BOLD signals in fMRI time series using multi-echo EPI. *Neuroimage* **60**, 1759–1770 (2012).
- Cox, R. W. AFNI: software for analysis and visualization of functional magnetic resonance neuroimages. *Comput. Biomed. Res.* **29**, 162–173 (1996).
- Papp, E. A., Leergaard, T. B., Calabrese, E., Johnson, G. A. & Bjaalie, J. G. Waxholm Space atlas of the Sprague Dawley rat brain. *Neuroimage* **97**, 374–386 (2014).
- Kim, S.-Y. et al. Stochastic electrotransport selectively enhances the transport of highly electrophoretic molecules. *Proc. Natl. Acad. Sci. USA* **112**, E6274–E6283 (2015).

53. Yun, D. H. et al. Ultrafast immunostaining of organ-scale tissues for scalable proteomic phenotyping. Preprint at bioRxiv <https://www.biorxiv.org/content/10.1101/660373v1> (2019).
54. Paxinos, G. & Watson, C. *The Rat Brain in Stereotaxic Coordinates, Compact Sixth Edition* (Academic Press, 2009).

Acknowledgements

This research was funded by NIH grant numbers R01 DA038642, R24 MH109081, UF1 NS107712 and U01 NS103470 and a grant from the MIT Simons Center for the Social Brain to A.J. S.G. was supported by an HHMI International Student Research Fellowship and Sheldon Razin Fellowship from the McGovern Institute for Brain Research. N.L. was supported by a Stanley Fahn Research Fellowship from the Parkinson's Disease Foundation. M.S. was the recipient of a Marie Curie Individual Fellowship from the European Commission. T.X. was a visiting student from the Beijing University of Chinese Medicine, funded by a scholarship from the China Scholarship Council. J.I.D. was supported by the Johnson & Johnson UROP Scholars Program at MIT. We are grateful to S. Lall and B. Sabatini for comments on the manuscript, and to A. Devor, I. Wickersham and H. Sullivan for conversations. We also thank L. McLain for providing CAD cells and T. Poulos of the University of California, Irvine and P. Ortiz de Montellano at the University of California, San Francisco for providing NOS constructs. R. Neve of the Massachusetts General Hospital is acknowledged for production of HSV vectors.

Author contributions

S.G., N.L., M.S., B.B.B. and A.J. designed the research. S.G., N.L., M.S., B.B.B., T.X., J.I.D. and U.D.S. performed the in vitro and in vivo experiments. K.X., N.D. and N.B.E. implemented the brain-clearing histology procedures under the direction of K.C. S.G., N.L., M.S. and A.J. analyzed the results. S.G., N.L. and A.J. wrote the paper.

Competing interests

The authors declare no competing interests.

Additional information

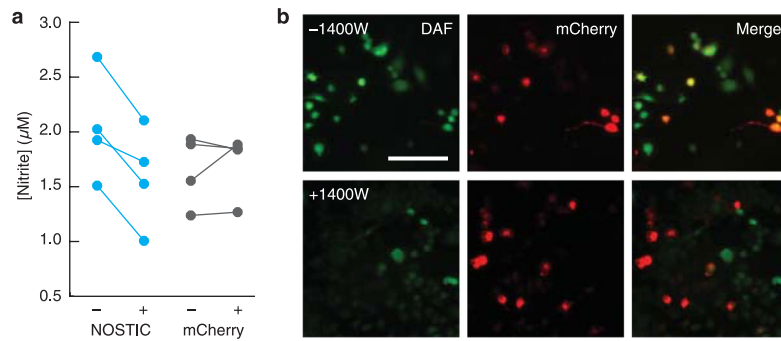
Extended data is available for this paper at <https://doi.org/10.1038/s41593-022-01014-8>.

Supplementary information The online version contains supplementary material available at <https://doi.org/10.1038/s41593-022-01014-8>.

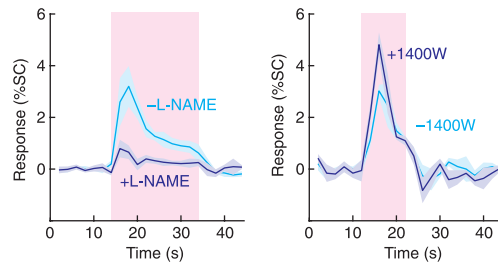
Correspondence and requests for materials should be addressed to Alan Jasanoff.

Peer review information *Nature Neuroscience* thanks Alan Koretsky, Jin Hyung Lee, and the other, anonymous, reviewer(s) for their contribution to the peer review of this work.

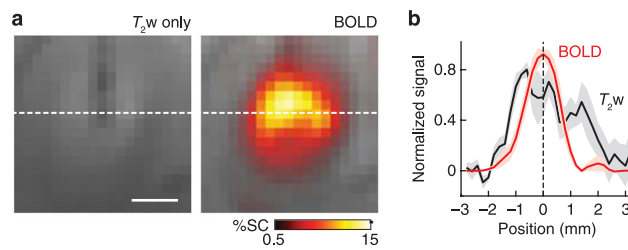
Reprints and permissions information is available at www.nature.com/reprints.



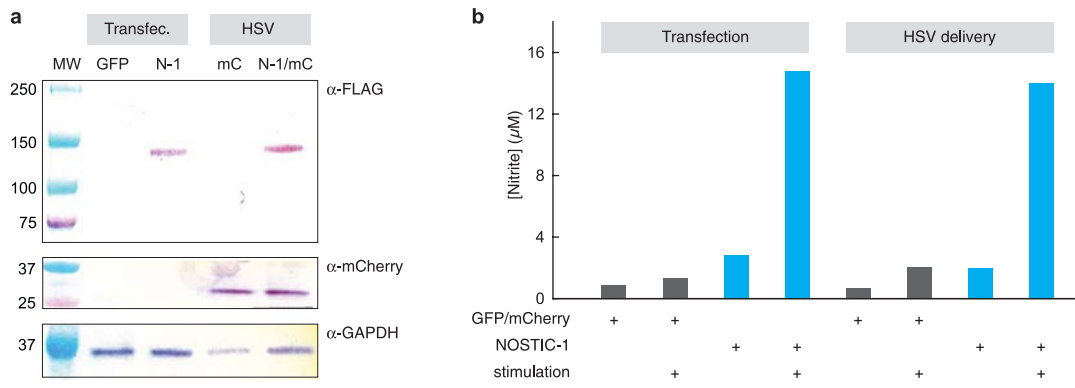
Extended Data Fig. 1 | NOSTIC functionality in a neuronal cell line. **a**, NOSTIC-1 fused to mCherry (cyan), as well as mCherry alone (gray), were expressed in CAD cells and stimulated with A23187 in the absence (-) or presence (+) of 100 μM 1400W; nitrite formation following NO release from the stimulated cells was measured for each condition. The effect of 1400W inhibition is significant for NOSTIC-expressing cells (paired t -test $p=0.013$, $n=4$) but not for control cells ($p=0.59$, $n=4$). **b**, NO production by A23187-stimulated CAD cells was visualized by staining with the fluorescent NO probe diaminofluorescein (DAF). NOSTIC-expressing cells indicated by red mCherry staining show higher levels of green DAF staining in the absence (top) than in the presence (bottom) of NOSTIC inhibition with 1400W. Scale bar = 200 μm . This experiment was performed twice.



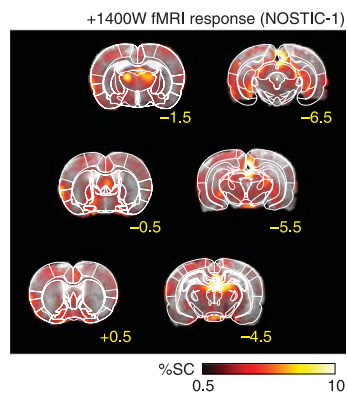
Extended Data Fig. 2 | Time courses of fMRI responses to forepaw stimulation. Mean fMRI signal time courses (% signal change) observed in the S1 forelimb region in response to stimulation of the contralateral paw (pink shaded region) in the presence vs. absence of L-NAME (left) or 1400W (right), corresponding to maps and mean response amplitudes reported in Fig. 1e. For arbitrary reasons, experiments testing effects of L-NAME and 1400W were performed with stimulation blocks of 20 s and 10 s, respectively, and differences in the response durations observed left vs. right arise from this fact.



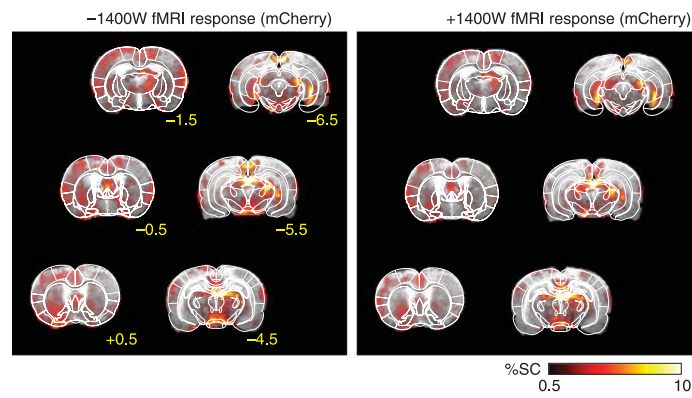
Extended Data Fig. 3 | Spatial extent of xenograft-induced hemogenetic responses. **a**, Left: Anatomical MRI showing T_2 -weighted (T_2w) contrast in the neighborhood of cell implantation for a representative animal from the experiments of main text Fig. 2. Right: Average BOLD contrast map (color) induced by A23187 stimulation in units of percent signal change (%SC), overlaid on a T_2 -weighted scan. **b**, Cross sections of the contrast patterns through the dotted line in panel a, with solid lines denoting means and shading denoting SEM across six animals' BOLD (red) and T_2w (black) signal changes. Full width at half maximum is 1.4 ± 0.1 mm for the hemogenetic BOLD responses, indicating point-spread function comparable to or less than conventional hemodynamic fMRI.



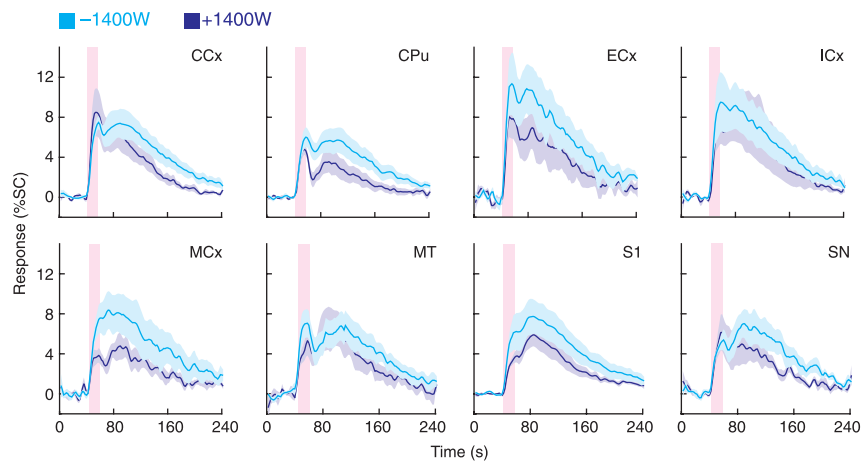
Extended Data Fig. 4 | Evaluation of HSV vectors in cell culture. a, Western blotting was used to analyze cells transfected (Transfec.) with GFP or NOSTIC-1 (N-1), along with cells infected with HSV encoding mCherry (mC) or NOSTIC-1-IRES-mCherry (N-1/mC). Expression and size of NOSTIC-1 was confirmed using blotting with an anti-FLAG tag (α-FLAG) antibody (top). Expression and size of mCherry in the HSV infected cells was assessed using an anti-mCherry antibody (α-mCherry, middle), and anti-glyceraldehyde 3-phosphate dehydrogenase (α-GAPDH) was used as a loading control (bottom). Relevant molecular weight (MW) markers labeled at left. Expected sizes: NOSTIC-1 140 kD, mCherry 29 kD, GAPDH 37 kD. **b**, Griess test measurement of nitrite production in the presence of cells transfected with GFP (gray) or NOSTIC-1 (cyan) or virally transduced with mCherry or NOSTIC-1, in the presence or absence of A23187 stimulation, as indicated. Only stimulated cells expressing NOSTIC-1 show strong evidence of stimulus-dependent NO production, as indicated by the Griess test results.



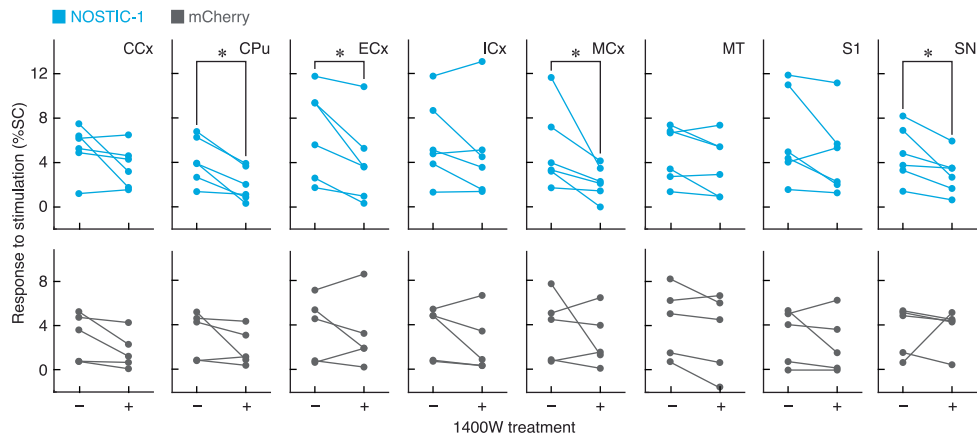
Extended Data Fig. 5 | LH stimulus responses in NOSTIC-expressing rats after 1400W treatment. Average fMRI responses to LH stimulation in the +1400W condition, among 6 animals infected with NOSTIC-encoding HSV, analogous to -1400W condition data in main text Fig. 3b. Significant responses with F -test $P \leq 0.01$ shown.



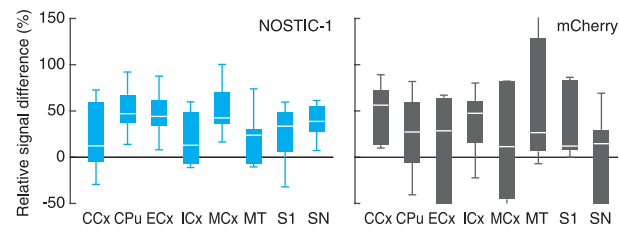
Extended Data Fig. 6 | Time courses of responses to LH stimulation in multiple ROIs. Average time courses of fMRI signals observed in eight ROIs in the presence and absence of 1400W, analogous to data of Fig. 3d. Pink boxes denote stimulation period. Shading denotes SEM over six animals each.



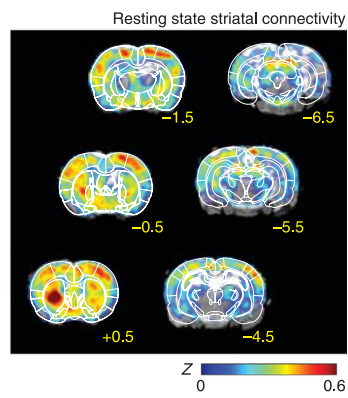
Extended Data Fig. 7 | LH stimulus responses in rats treated with control HSV vectors. Average fMRI responses to LH stimulation in the -1400W (left) and +1400W (right) conditions, among 5 animals infected with mCherry-encoding HSV, corresponding to difference maps shown in main text Fig. 3c. Significant responses with F -test $P \leq 0.01$ shown.



Extended Data Fig. 8 | 1400W-dependent fMRI amplitudes observed in multiple ROIs. Absolute fMRI response amplitudes observed in each of eight ROIs examined in NOSTIC and control mCherry HSV-treated animals, analogous to data presented in Fig. 3f. 1400W-dependent effects in CPu, ECx, MCx, and SN are all significant with paired *t*-test $*P \leq 0.05$ ($n = 6$).



Extended Data Fig. 9 | Relative changes in fMRI amplitudes upon 1400W treatment. ROI-averaged fMRI amplitudes from the experiments of Fig. 3 were used to compute relative signal differences as $100 \times (pre - post)/pre$, where *pre* and *post* are the fMRI amplitudes observed before and after 1400W application in each rat. Results are shown as box plots for NOSTIC-1-treated (left, $n = 6$) and control mCherry-treated (right, $n = 5$) animals. Box plots denote median (center line), first quartiles (boxes), and full range (whiskers) over animals. NOSTIC results are significant in CPu, ECx, MCx, and SN (t-test $P \leq 0.008$); control results are significant in CCx (t-test $P = 0.037$).



Extended Data Fig. 10 | Resting-state functional connectivity to CPu. A map of Z-transformed correlation coefficients relating resting state fMRI signal in a striatal seed region to voxels across the rest of the brain.

Reporting Summary

Nature Portfolio wishes to improve the reproducibility of the work that we publish. This form provides structure for consistency and transparency in reporting. For further information on Nature Portfolio policies, see our [Editorial Policies](#) and the [Editorial Policy Checklist](#).

Statistics

For all statistical analyses, confirm that the following items are present in the figure legend, table legend, main text, or Methods section.

n/a Confirmed

- The exact sample size (n) for each experimental group/condition, given as a discrete number and unit of measurement
- A statement on whether measurements were taken from distinct samples or whether the same sample was measured repeatedly
- The statistical test(s) used AND whether they are one- or two-sided
Only common tests should be described solely by name; describe more complex techniques in the Methods section.
- A description of all covariates tested
- A description of any assumptions or corrections, such as tests of normality and adjustment for multiple comparisons
- A full description of the statistical parameters including central tendency (e.g. means) or other basic estimates (e.g. regression coefficient) AND variation (e.g. standard deviation) or associated estimates of uncertainty (e.g. confidence intervals)
- For null hypothesis testing, the test statistic (e.g. F , t , r) with confidence intervals, effect sizes, degrees of freedom and P value noted
Give P values as exact values whenever suitable.
- For Bayesian analysis, information on the choice of priors and Markov chain Monte Carlo settings
- For hierarchical and complex designs, identification of the appropriate level for tests and full reporting of outcomes
- Estimates of effect sizes (e.g. Cohen's d , Pearson's r), indicating how they were calculated

Our web collection on [statistics for biologists](#) contains articles on many of the points above.

Software and code

Policy information about [availability of computer code](#)

Data collection

Data analysis

For manuscripts utilizing custom algorithms or software that are central to the research but not yet described in published literature, software must be made available to editors and reviewers. We strongly encourage code deposition in a community repository (e.g. GitHub). See the Nature Portfolio [guidelines for submitting code & software](#) for further information.

Data

Policy information about [availability of data](#)

All manuscripts must include a [data availability statement](#). This statement should provide the following information, where applicable:

- Accession codes, unique identifiers, or web links for publicly available datasets
- A description of any restrictions on data availability
- For clinical datasets or third party data, please ensure that the statement adheres to our [policy](#)

Source data for Figures 1-5 and associated Extended Data Figures are provided with this submission. The MRI atlas used for this study was downloaded from <https://www.nitrc.org/projects/whs-sd-atlas>.

Field-specific reporting

Please select the one below that is the best fit for your research. If you are not sure, read the appropriate sections before making your selection.

Life sciences Behavioural & social sciences Ecological, evolutionary & environmental sciences

For a reference copy of the document with all sections, see [nature.com/documents/nr-reporting-summary-flat.pdf](https://www.nature.com/documents/nr-reporting-summary-flat.pdf)

Life sciences study design

All studies must disclose on these points even when the disclosure is negative.

Sample size	Experiments were performed on multiple samples or animals to ensure reproducibility and permit group-level comparisons.
Data exclusions	Experimental sessions that suffered from major technical failures were excluded from analysis.
Replication	Experiments were performed with multiple successful replicates as noted throughout the text and captions. Standard statistical methods were used to accept or reject null hypotheses of no effect.
Randomization	The study did not involve comparison of subjects with different treatment histories; randomization was therefore not relevant.
Blinding	Researchers were not blinded to experimental conditions.

Reporting for specific materials, systems and methods

We require information from authors about some types of materials, experimental systems and methods used in many studies. Here, indicate whether each material, system or method listed is relevant to your study. If you are not sure if a list item applies to your research, read the appropriate section before selecting a response.

Materials & experimental systems

Methods

n/a	Involved in the study	n/a	Involved in the study
<input type="checkbox"/>	<input checked="" type="checkbox"/> Antibodies	<input checked="" type="checkbox"/>	<input type="checkbox"/> ChIP-seq
<input type="checkbox"/>	<input checked="" type="checkbox"/> Eukaryotic cell lines	<input checked="" type="checkbox"/>	<input type="checkbox"/> Flow cytometry
<input checked="" type="checkbox"/>	<input type="checkbox"/> Palaeontology and archaeology	<input type="checkbox"/>	<input checked="" type="checkbox"/> MRI-based neuroimaging
<input type="checkbox"/>	<input checked="" type="checkbox"/> Animals and other organisms		
<input checked="" type="checkbox"/>	<input type="checkbox"/> Human research participants		
<input checked="" type="checkbox"/>	<input type="checkbox"/> Clinical data		
<input checked="" type="checkbox"/>	<input type="checkbox"/> Dual use research of concern		

Antibodies

Antibodies used	Primary antibodies: goat anti-mCherry (LSBio LS-C204207, 1:200), rabbit anti-mCherry (Abcam ab167453, 1:200), rabbit anti-c-Fos (Synaptic Systems 226008, 1:500), goat anti-IBA-1 (Abcam ab5067, 1:500), rabbit anti-nitrotyrosine (MilliporeSigma AB5411, 1:200). Secondary antibodies: donkey anti-rabbit IgG tagged with Alexa Fluor 594 (Thermo Fisher A-21207), donkey anti-goat IgG tagged with Alexa Fluor 488 (Thermo Fisher A-11055), donkey anti-goat IgG tagged with Alexa Fluor 594 (Thermo Fisher A-11058), or donkey anti-rabbit IgG tagged with Alexa Fluor 488 (Thermo Fisher A-21206).
Validation	Only commercial antibodies from respected sources were used; validation by the supplier was assumed.

Eukaryotic cell lines

Policy information about [cell lines](#)

Cell line source(s)	HEK 293FT cells and 293-F Freestyle cells from Thermo Fisher, CAD cells were produced by Dona Chikaraishi and colleagues (Department of Neurobiology, Duke University)
Authentication	Commercially available cell lines were not further validated in-house.
Mycoplasma contamination	Cell lines tested negative for mycoplasma contamination in the MycoAlert assay (Lonza, Walkersville, MD, USA).
Commonly misidentified lines (See ICLAC register)	None of these were used.

Animals and other organisms

Policy information about [studies involving animals](#); [ARRIVE guidelines](#) recommended for reporting animal research

Laboratory animals	Male Sprague-Dawley rats (200-250 g, 7-8 weeks old)
Wild animals	The study did not involve wild animals.
Field-collected samples	The study did not involve samples collected from the field.
Ethics oversight	All procedures were carried out in strict compliance with National Institutes of Health guidelines, under oversight of the Committee on Animal Care at the Massachusetts Institute of Technology as part of protocol number 0721-059-24.

Note that full information on the approval of the study protocol must also be provided in the manuscript.

Magnetic resonance imaging

Experimental design

Design type	block design
Design specifications	Functional imaging with forepaw stimulation consisted of six blocks of 3 mA 1 ms pulses repeated at 9 Hz for 10-20 s alternating with 40-80 s of rest. Functional imaging of HSV-transfected rats included two minutes of baseline image acquisition followed by five cycles of electrical stimulation, each consisting of 16 s LH stimulation followed by 5 min of rest.
Behavioral performance measures	N/A

Acquisition

Imaging type(s)	Functional and structural
Field strength	9.4 Telsa
Sequence & imaging parameters	A T2*-weighted echo planar imaging (EPI) sequence was used for detection of stimulus induced BOLD contrast, with BW = 200 kHz, TE = 16 ms, FA = 90, TR = 2s, FOV = 2.56 × 1.28 cm, in-plane resolution 400 × 400 μm, and slice thickness = 1 mm.
Area of acquisition	For functional imaging with forepaw stimulation, six coronal brain slices ranging from Bregma -1.5 mm to +3.5 mm were imaged. For functional imaging with LH stimulation, twelve coronal brain slices ranging from Bregma -6.5 mm to +2.5 mm were imaged. Brain regions around the stimulation site (Bregma -2.5 mm to Bregma -3.5 mm) on LH, where SNR of the images are affected by the implantation of the stimulation electrode, were not used for analysis.
Diffusion MRI	<input type="checkbox"/> Used <input checked="" type="checkbox"/> Not used

Preprocessing

Preprocessing software	Functional imaging time series were preprocessed using AFNI in steps that included slice timing correction, motion correction using a least squares rigid-body volume registration algorithm, voxel-wise intensity normalization, spatial smoothing with Gaussian spatial kernel of 0.5 mm full width at half maximum, and spatial resampling to double the image matrix size. Segmentation of brain from non-brain voxels was performed in MATLAB (Mathworks).
Normalization	High-resolution anatomical images of each animal were registered to a Waxholm coordinate space rat brain MRI atlas. Preprocessed time series were then co-registered onto the previously atlas-aligned anatomical images. Linear transformation 3dAllineate in AFNI was used for registration with the cost function of Local Pearson Correlation Abs (LPA) and/or Least Squares (LS).
Normalization template	The template used for normalization/registration is the Waxholm coordinate space rat brain MRI atlas. ROIs were defined with respect to Paxinos and Waxholm atlases.
Noise and artifact removal	AFNI functions were used for motion correction.
Volume censoring	No censoring was applied.

Statistical modeling & inference

Model type and settings	Comparisons of mean fMRI amplitudes, durations, and regression coefficients were performed using Student's t-test. Significance of regressor-dependent contributions in GLM analyses, including assessment of the proportionality between dopamine and BOLD signals, was evaluated using F-test. Differences between correlation coefficients were evaluated using Fisher's Z-test.
-------------------------	---

Effect(s) tested

(1) fMRI responses of A23187 stimulation on the cells expressing NOSTIC-1 or GFP implanted to the striatum, with or without 1400W treatment. (2) fMRI responses to the left forepaw stimulation were assessed, both before and after treatment with L-NAME, an inhibitor of nNOS, and 1400W, the inhibitor of NOSTIC-1, respectively. (3) fMRI responses to LH stimulation were assessed, both before and after treatment with 1400W, the inhibitor of NOSTIC-1.

Specify type of analysis: Whole brain ROI-based Both

Anatomical location(s)

High-resolution anatomical images of each animal were registered to a Waxholm coordinate space rat brain MRI atlas. ROIs used for subsequent analyses were defined with respect to Waxholm and Paxinos rat atlases.

Statistic type for inference
(See [Eklund et al. 2016](#))

Voxel-wise, ROI-wise

Correction

Statistical thresholds noted throughout.

Models & analysis

n/a | Involved in the study

- Functional and/or effective connectivity
 Graph analysis
 Multivariate modeling or predictive analysis

Functional and/or effective connectivity

Linear regression